

Private, fair and accurate: Training large-scale, privacy-preserving AI models in medical imaging*

Soroosh Tayebi Arasteh^{1,+}, Alexander Ziller^{2,3,+}, Christiane Kuhl¹, Marcus Makowski², Sven Nebelung¹, Rickmer Braren², Daniel Rueckert³, Daniel Truhn^{1,x}, and Georgios Kaissis^{2,3,4,5,x,*}

¹Department of Diagnostic and Interventional Radiology, University Hospital RWTH Aachen, Aachen, Germany.

²Institute of Diagnostic and Interventional Radiology, Technical University of Munich, Munich, Germany.

³Artificial Intelligence in Healthcare and Medicine, Technical University of Munich, Munich, Germany.

⁴Department of Computing, Imperial College London, London, United Kingdom.

⁵Institute for Machine Learning in Biomedical Imaging, Helmholtz-Zentrum Munich, Neuherberg, Germany.

*
g.kaissis@tum.de

⁺These authors contributed equally to this work

^xThese authors contributed equally to this work

January 26, 2024

Abstract

Artificial intelligence (AI) models are increasingly used in the medical domain. However, as medical data is highly sensitive, special precautions to ensure its protection are required. The gold standard for privacy preservation is the introduction of differential privacy (DP) to model training. Prior work indicates that DP has negative implications on model accuracy and fairness, which are unacceptable in medicine and represent a main barrier to the widespread use of privacy-preserving techniques. In this work, we evaluated the effect of privacy-preserving training of AI models regarding accuracy and fairness compared to non-private training. For this, we used two datasets: (1) A large dataset ($N = 193\,311$) of high quality clinical chest radiographs, and (2) a dataset ($N = 1\,625$) of 3D abdominal computed tomography (CT) images, with the task of classifying the presence of pancreatic ductal adenocarcinoma (PDAC). Both were retrospectively collected and manually labeled by experienced radiologists. We then compared non-private deep convolutional neural networks (CNNs) and privacy-preserving (DP) models with respect to privacy-utility trade-offs measured as area under the receiver-operator-characteristic curve (AUROC), and privacy-fairness trade-offs, measured as Pearson's r or Statistical Parity Difference. We found that, while the privacy-preserving trainings yielded lower accuracy, they did largely not amplify discrimination against age, sex or co-morbidity. Our study shows that –under the challenging realistic circumstances of a real-life clinical dataset– the privacy-preserving training of diagnostic deep learning models is possible with excellent diagnostic accuracy and fairness.

1 Introduction

The development of artificial intelligence (AI) systems for medical applications represents a delicate trade-off: On the one hand, diagnostic models must offer high accuracy and certainty, as well as treat different patient

*Accepted by Communications Medicine. 2024. Nature Portfolio.

groups equitably and fairly. On the other hand, clinicians and researchers are subject to ethical and legal responsibilities towards the patients whose data is used for model training. In particular, when diagnostic models are published to third parties whose intentions are impossible to verify, care must be undertaken to ascertain that patient privacy is not compromised. Privacy breaches can occur, e.g. through data reconstruction, attribute inference or membership inference attacks against the shared model [1]. Federated learning [2, 3, 4] has been proposed as a tool to address some of these problems. However, it has become evident that training data can be reverse-engineered piecemeal from federated systems, rendering them just as vulnerable to the aforementioned attacks as centralized learning [5]. Thus, it is apparent that formal privacy preservation methods are required to protect the patients whose data is used to train diagnostic AI models. The gold standard in this regard is differential privacy (DP) [6].

Most, if not all, currently deployed machine learning models are trained without any formal privacy-preservation technique. It is especially crucial to employ such techniques in federated scenarios, where much more granular information about the training process can be extracted, or even the training process itself can be manipulated by a malicious participant [7, 8]. Moreover, trained models can be attacked to extract training data through so-called model inversion attacks [9, 10, 11]. We also note that such attacks work better if the models have been trained on less data, which is especially concerning since even most FDA-approved AI algorithms have been trained on fewer than 1 000 cases [12]. Creating a one-to-one correspondence between a successful attack and the resulting “privacy risk” requires a case-by-case consideration. The legal opinion (e.g., the GDPR) seems to have converged on the notion of singling out/ re-identification. Even from the aspect of newer legal frameworks, such as the EU AI act, which demand “risk moderation” rather than directly specifying “privacy requirements”, DP can be seen as the optimal tool as it can quantitatively bound both the risk of membership inference (MI) [13, 14] and data reconstruction [15]. Moreover, this was also shown empirically for both aforementioned attack classes [16, 17, 18, 19]. It is also known that DP, contrary to de-identification procedures such as k -anonymity, provably protects against the notion of singling out [20, 21].

DP is a formal framework encompassing a collection of techniques to allow analysts to obtain insights from sensitive datasets while guaranteeing the protection of individual data points within them. DP thus is a property of a data processing system which states that the results of a computation over a sensitive dataset must be approximately identical whether or not any single individual was included or excluded from the dataset. Formally, a randomised algorithm (mechanism) $\mathcal{M} : \mathcal{X} \rightarrow \mathcal{Y}$ is said to satisfy (ϵ, δ) -DP if, for all pairs of databases $D, D' \in \mathcal{X}$ which differ in one row and all $S \subseteq \mathcal{Y}$, the following holds:

$$\Pr(\mathcal{M}(D) \in S) \leq e^\epsilon \Pr(\mathcal{M}(D') \in S) + \delta, \quad (1)$$

where the guarantee is given over the randomness of \mathcal{M} and holds equally when D and D' are swapped. In more intuitive terms, DP is a guarantee given from a data processor to a data owner that the risks of adverse events which can occur due to the inclusion of their data in a database are bounded compared to the risks of such events when their data is not included. The parameters ϵ and δ together form what is typically called a *privacy budget*. Higher values of ϵ and δ correspond to a looser privacy guarantee and *vice versa*. With some terminological laxity, ϵ can be considered a measure of the *privacy loss* incurred, whereas δ represents a (small) probability that this privacy loss is exceeded. For deep learning workflows, δ is set to around the inverse of the database size. We note that, although mechanisms exist where δ denotes a catastrophic privacy degradation probability, the sampled Gaussian mechanism used to train neural networks does not exhibit this behaviour. The fact that quantitative privacy guarantees can be computed over many iterations (*compositions*) of complex algorithms like the ones used to train neural networks is unique to DP. This process is typically referred to as *privacy accounting*. Applied to neural network training, the randomization required by DP is ensured through the addition of calibrated Gaussian noise to the gradients of the loss function computed for each individual data point after they have been clipped in ℓ_2 -norm to ensure that their magnitude is bounded [22], where the clipping threshold is an additional hyperparameter in the training process (see Figure 1).

DP does not only offer formal protection, but several works have also empirically shown the connection between the privacy budget and the success of membership inference [16] and data reconstruction attacks [17, 23, 19]. We note that absolute privacy (i.e. zero risk) is only possible if no information is present [24]. This is, for example, the case in encryption methods, which are perfectly private as long as data is not decrypted. Note that training models e.g. via homomorphic encryption does, however, not offer such perfect privacy guarantees, as the information learned by the model is actually revealed at inference time through the

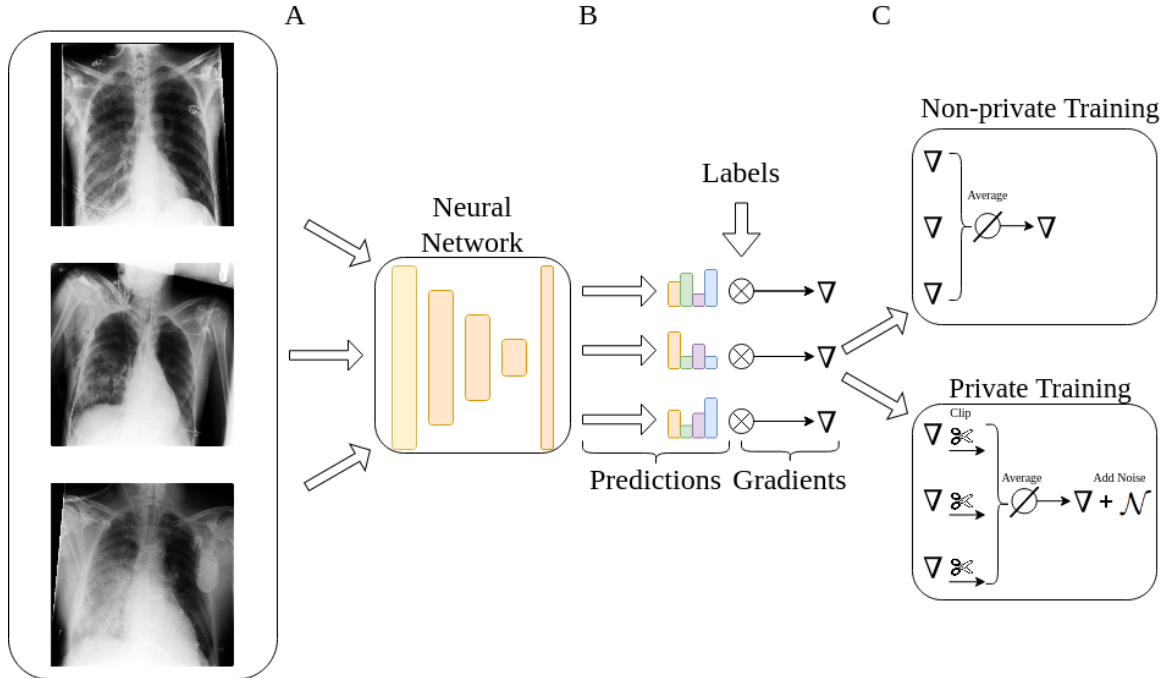


Figure 1: Differences between the private and non-private training process of a neural network. (A) Images from a dataset are fed to a neural network and predictions are made. (B) From the predictions and the ground truth labels, the gradient is calculated via backpropagation. (C, upper panel) In normal training all gradients are averaged and an update step is performed. (C, lower panel) In private training, each per-sample gradient is clipped to a predetermined ℓ_2 -norm, averaged and noise proportional to the norm is added. This ensures that the information about each sample is upper-bounded and perturbed with sufficient noise.

model’s predictions. Thus, without the protection of differential privacy, no formal barrier stands between the sensitive data and an attacker (beyond potential imperfections of the attack algorithm, which are usually not controllable *a priori*). DP offers the ability to upper-bound the risk of successful privacy attacks while still being able to draw conclusions from the data. Determining the exact privacy budget is challenging, as it is a matter of *policy*. The technical perspective can provide insight into the appropriate budget level, as it is possible to quantify the risk of a successful attack at a given privacy budget compared to the model utility that can be achieved. The trade-offs between model utility and privacy preservation are also a matter of ethical, societal and political debate. The utilisation of DP also creates two fundamental trade-offs: The first is a “privacy-utility trade-off”, i.e., a reduction in diagnostic accuracy when stronger privacy guarantees are required [25, 26]. The other trade-off is between privacy and fairness. Intuitively, the fact that AI models learn proportionally less about under-represented patient groups [27] in the training data is amplified by DP, leading to demographic disparity in the model’s predictions or diagnoses [28]. Both of these trade-offs are delicate in sensitive applications, such as medical ones, as it is not acceptable to have wrong diagnoses or to discriminate against a certain patient group.

In this work, we aim to elucidate the connection between using formal privacy techniques and the fairness towards underrepresented groups in the sensitive setting of medical use-cases. This is an important prerequisite for the deployment of ethical AI algorithms in such sensitive areas. However, so far, prior work is limited to benchmark computer vision datasets [29, 30]. We thus contend that the widespread use of privacy-preserving machine learning requires testing under real-life circumstances. In the current study, we perform the first in-depth investigation into this topic. Concretely, we utilize a large clinical database of radiologist-labeled radiographic images, which has previously been used to train an expert-level diagnostic AI model, but otherwise not been curated or pre-processed for private training in any way. Furthermore, we analyze a dataset of abdominal 3D computed tomography (CT) images, where we classify the presence of a pancreatic ductal adenocarcinoma (PDAC). This mirrors the type of datasets available at clinical institutions.

In this setting, we then study the extent of privacy-utility and privacy-fairness trade-offs in training advanced computer vision architectures. Our main contributions can be summarized as follows:

1. We study the diagnostic accuracy ramifications of differentially private deep learning on two curated databases of medically relevant use-cases. We reach 97% of the non-private AUROC on the UKA-CXR dataset through the utilization of transfer learning on public datasets and careful choice of architecture. On the PDAC dataset, our private model at $\epsilon = 8.0$ is not statistically significantly inferior compared to the non-private baseline.
2. We investigate the fairness implications of differentially private learning with respect to key demographic characteristics such as sex, age and co-morbidity. We find that – while differentially private learning has a mild fairness effect – it does not introduce significant discrimination concerns compared to non-private training, especially at the intermediate privacy budgets typically used in large-scale applications.

Prior work The need for the use of differential privacy (DP) has been illustrated by Packhäuser et al. [31], who showed that it is trivial to match chest x-rays of the same patient, which directly enables re-identification attacks; this was similarly shown in tabular databases by Narayanan et al. [32]. The training of deep neural networks on medical data with DP has so far not been widely investigated. Li et al. [33] investigated privacy-utility trade-offs in the combination of advanced federated learning schemes and DP methods on a brain tumor segmentation dataset. They find that DP introduces a considerable reduction in model accuracy in the given setting. Hatamizadeh et al. [23] illustrated that the use of federated learning alone is unsafe, as training data can be reconstructed in such settings. Ziegler et al. [34] reported similar findings when evaluating privacy-utility trade-offs for a chest x-ray classification on a public dataset. These results also align with our previous work [17], where we demonstrated the utilization of a suite of privacy-preserving techniques for pneumonia classification in pediatric chest x-rays. However, the focus of this study was not to elucidate privacy-utility or privacy-fairness trade-offs, but to showcase that federated learning workflows can be used to train diagnostic AI models with good accuracy on decentralized data while minimizing data privacy and governance concerns. Moreover, we demonstrated that empirical data reconstruction attacks are thwarted by the utilization of differential privacy. In addition, the work did not consider differential diagnosis but only coarse-label classification into normal vs. bacterial or viral pneumonia.

To the best of our knowledge, our study is the first work to investigate the use of differential privacy in the training of complex diagnostic AI models on a real-world dataset of this magnitude (nearly 200 000 samples) and a 3D classification task, and to include an extensive evaluation of privacy-utility and privacy-fairness trade-offs.

Our results are of interest to medical practitioners, deep learning experts in the medical field and regulatory bodies such as legislative institutions, institutional review boards and data protection officers and we undertook specific care to formulate our main lines of investigation across the important axes delineated above, namely the provision of objective metrics of diagnostic accuracy, privacy protection and demographic fairness towards diverse patient subgroups.

2 Materials and Methods

2.1 Patient Cohorts

We employed UKA-CXR [35, 36], a large cohort of chest radiographs. The dataset consists of $N = 193\,311$ frontal CXR images of 54 176 patients, all manually labeled by radiologists. The available labels include: pleural effusion, pneumonic infiltrates, and atelectasis, each separately for right and left lung, congestion, and cardiomegaly. The labeling system for cardiomegaly included five classes “normal”, “uncertain”, “borderline”, “enlarged”, and “massively enlarged”. For the rest of the labels, five classes of “negative”, “uncertain”, “mild”, “moderate”, and “severe” were used. Data were split into $N = 153\,502$ training and $N = 39\,809$ test images using patient-wise stratification, but otherwise completely random allocation [35, 36]. There was no overlap between the training and test sets. Supplementary Table 2 shows the statistics of the dataset, which are further visualized in Supplementary Figures 7 and 8.

In addition, we used an in-house dataset at Klinikum Rechts der Isar of 1 625 abdominal CT scans from unique, consecutive patients, of which 867 suffered from pancreatic ductal adenocarcinoma (PDAC) (positive)

and 758 were a control group without a tumor (negative). We split the dataset into 975 train and 325 validation and test images respectively. During splitting we maintained the ratio of positive and negative samples in all subsets.

2.2 Data Pre-processing

We resized all images of the UKA-CXR dataset to (512×512) pixels. Afterward, a normalization scheme as described previously by Johnson et al. [37] was utilized by subtracting the lowest value in the image, dividing by the highest value in the shifted image, truncating values, and converting the result to an unsigned integer, i.e., in the range of $[0, 255]$. Finally, we performed histogram equalization by shifting pixel values towards 0 or towards 255 such that all pixel values 0 through 255 have approximately equal frequencies [37].

We selected a binary classification paradigm for each label. The “negative” and “uncertain” classes (“normal” and “uncertain” for cardiomegaly) were treated as negative, while the “mild”, “moderate”, and “severe” classes (“borderline”, “enlarged”, and “massively enlarged” for cardiomegaly) were treated as positive.

For the PDAC dataset, we clipped the voxel density values of all CT scans to an abdominal window from -150 to 250 Hounsfield units and resized to a shape of $224 \times 224 \times 128$ voxels.

2.3 Deep Learning Process

2.3.1 Network Architecture

For both datasets, we employed the ResNet9 architecture introduced in [38] as our classification architecture. For the UKA-CXR dataset, images were expanded to $(512 \times 512 \times 3)$ for compatibility with the neural network architecture. The final linear layer reduces the (512×1) output feature vectors to the desired number of diseases to be predicted, i.e., 8. The sigmoid function was utilized to convert the output predictions to individual class probabilities. The full network contained a total of 4.9 million trainable parameters. For the PDAC dataset, we used the conversion proposed by Yang et al. [39] to convert the model to be applicable to 3D data, which in brief applies 2D-convolutional filters along axial, coronal, and sagittal axes separately. Our utilized ResNet9 network employs the modifications proposed by Klause et al. [38] and by He et al. [40]. Batch Normalization [41] is incompatible with DP-SGD, as per-sample gradients are required, and batch normalization inherently intermixes information of all images in one batch. Hence, we used group normalization [42] layers instead with 32 groups to be compatible with DP processing. For the CXR dataset we pretrained the network on the MIMIC Chest X-ray JPG dataset v2.0.0 (MIMIC-CXR), [43] consisting of $N = 210\,652$ frontal images. All training hyperparameters were selected empirically based on their validation accuracy, while no systematic/automated hyperparameter tuning was conducted.

2.3.2 Non-DP Training

For the UKA-CXR dataset, the Rectified Linear Unit (ReLU) [44] was chosen as the activation function in all layers. We performed data augmentation during training by applying random rotation in the range of $[-10, 10]$ degrees and medio-lateral flipping with a probability of 0.50. The model was optimized using the NAdam [45] optimizer with a learning rate of $5 \cdot 10^{-5}$. The binary weighted cross-entropy with inverted class frequencies of the training data was selected as the loss function. The training batch size was chosen to be 128. In the PDAC dataset, we used an unweighted binary cross-entropy loss as well as the NAdam optimizer with a learning rate of $2 \cdot 10^{-4}$.

2.3.3 DP Training

For UKA-CXR we chose Mish [46] as the activation function in all layers. No data augmentation was performed during DP training as we found further data augmentation during training to be harmful to accuracy. All models were optimized using the NAdam [45] optimizer with a learning rate of $5 \cdot 10^{-4}$. The binary weighted cross-entropy with inverted class frequencies of the training data was selected as the loss function. The maximum allowed gradient norm was chosen to be 1.5 and the network was trained for 150 epochs for each chosen privacy budget. Each point in the batch was sampled with a probability of $8 \cdot 10^{-4}$ (128 divided by $N = 153\,502$). For the PDAC dataset, we chose a clipping norm of 1.0, $\delta = 0.001$ and a

sampling rate of 0.31 (512/1625). In both cases, the noise multiplier was calculated such that for a given number of training steps, sampling rate, and maximum gradient norm the privacy budget was reached on the last training step. For the UKA-CXR dataset, the indicated privacy guarantees are “per record” since some patients have more than one image, while for the PDAC datasets, they are “per individual”.

2.4 Quantitative Evaluation and Statistical Analysis

The area under the receiver-operator-characteristic curve (AUROC) was utilized as the primary evaluation metric. We report the average AUROC over all the labels for each experiment. The individual AUROC as well as all other evaluation metrics of individual labels are reported in the supplemental material (Supplementary Tables 3–9). For the UKA-CXR test set, we used bootstrapping with 1 000 redraws for each measure to determine the statistical spread [47]. For calculating sensitivity, specificity, and accuracy, a threshold was chosen according to Youden’s criterion [48], i.e., the threshold that maximized (true positive rate - false positive rate).

To evaluate the correlation between results of data subsets and their sample size, Pearson’s r coefficient was used. To analyze fairness between subgroups, the statistical parity difference [49] was used which is defined as $P(\hat{Y} = 1|C = \text{Minority}) - P(\hat{Y} = 1|C = \text{Majority})$ where $\hat{Y} = 1$ represents correct model predictions and C is the group in question. Intuitively, it is the difference in classification accuracy between the minority and majority class and thus is optimally zero. Values larger than zero mean that there is a benefit for the minority class, while values smaller than zero mean that the minority class is discriminated against.

3 Results

3.1 High classification accuracy is attainable despite stringent privacy guarantees

Table 1 shows an overview of our results for all subgroups. Supplementary Tables 3–9 show the per-diagnosis evaluation results for non-DP and DP training for different ϵ values. On the UKA-CXR dataset our non-private model achieves an AUROC of 89.71% over all diagnoses. It performs best on pneumonic infiltration on the right (AUROC=94%) while struggling the most to accurately classify cardiomegaly (AUROC=84%). Training with DP decreases all results slightly yet significantly (Hanley & McNeil-test p -value < 0.001) and achieves an overall AUROC of 87.36%. The per-diagnosis performance ranges from 92% (pleural effusion right) to 81% AUROC (congestion). We next consider classification performance at a very strong level of privacy protection (i.e., at $\epsilon < 1$). Here, at an ϵ -budget of only 0.29, our model achieves an average AUROC of 83.13% over all diagnoses. A visual overview is displayed in Figure 3, which shows the average AUROC, accuracy, sensitivity, and specificity values over all labels.

On the PDAC dataset, we found that, while non-private training achieved almost perfect results on the test set the loss in utility for private training at $\epsilon = 8$ is statistically non-significant (Hanley & McNeil-test p -value: 0.34) compared to non-private training. Again, with lower privacy budgets, model utility decreases, but even at a very low privacy budget of $\epsilon = 1.06$, we observe an average AUC score of 95.58%.

Moreover, for UKA-CXR, the use of pre-training helps to boost model performance and reduce the amount of additional information the model needs to learn “from scratch” and consequently reduces the privacy budgets required (refer to Supplementary Figure 9). This appears to primarily benefit the under-represented groups in the dataset. Conversely, non-private training, whether initialized with pre-training weights or trained from scratch, tends to yield comparable diagnostic results, as the latter network can leverage a greater amount of information. These findings are in line with the observations on the PDAC dataset (where no pretrained weights were available), namely that, at low privacy budgets, specific patient groups suffer a higher discrimination.

For the purpose of further generalization, we replicated the experiments using three other network architectures. All three models displayed a trend consistent with the utility penalties we observed for ResNet9 in both DP and non-DP training (see Supplementary Figure 10). For further details, we refer to Appendix A.1.

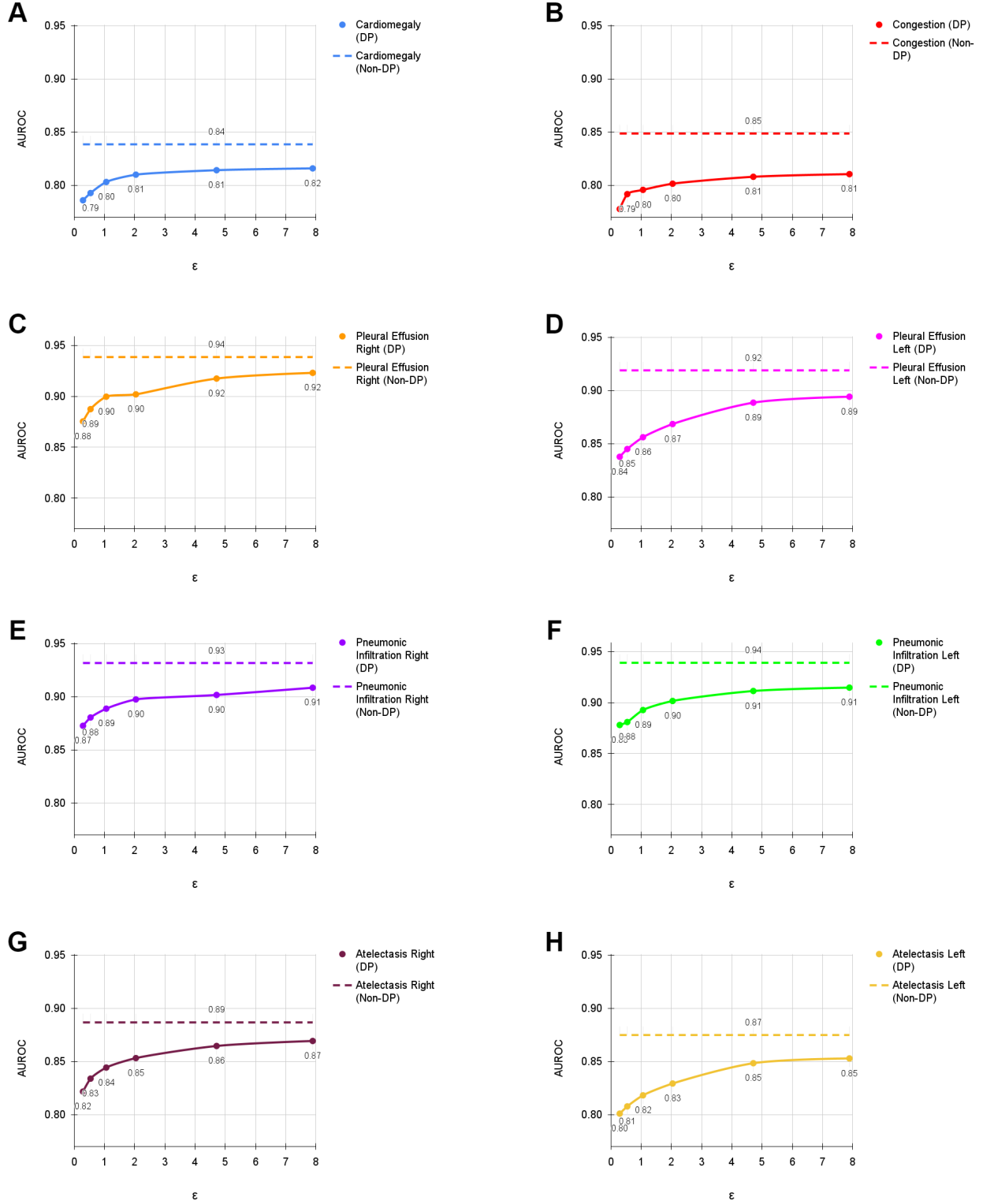


Figure 2: Evaluation results of training with DP and without DP with different ϵ values for $\delta = 6 \cdot 10^{-6}$. The results show the individual AUROC values for (A) cardiomegaly, (B) congestion, (C) pleural effusion right, (D) pleural effusion left, (E) pneumonic infiltration right, (F) pneumonic infiltration left, (G) atelectasis right, and (H) atelectasis left tested on $N = 39\,809$ test images. The training dataset includes $N = 153\,502$ images. Dashed lines correspond to the non-private training results.

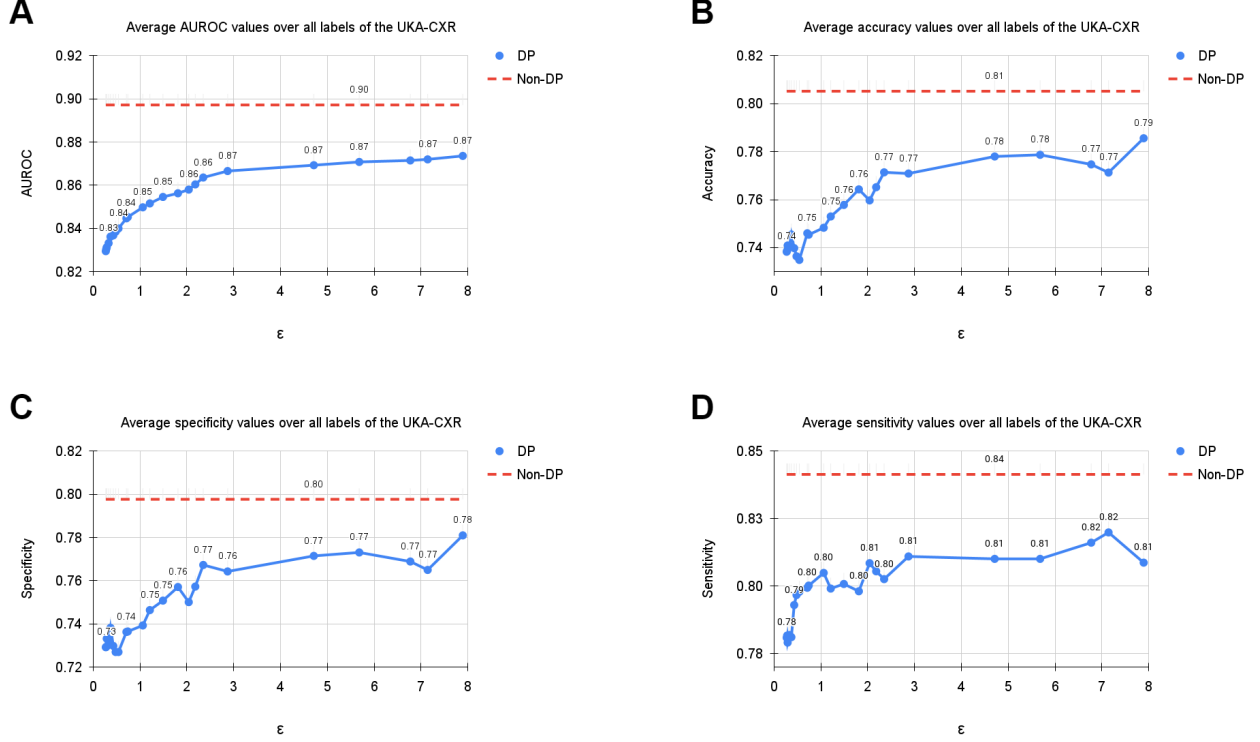


Figure 3: Average results of training with DP with different ϵ values for $\delta = 6 \cdot 10^{-6}$. The curves show the average (A) area-under-the-receiver-operator-curve (AUROC), (B) accuracy, (C) specificity, and (D) sensitivity values over all labels, including cardiomegaly, congestion, pleural effusion right, pleural effusion left, pneumonic infiltration right, pneumonic infiltration left, atelectasis right, and atelectasis left tested on $N = 39\,809$ test images. The training dataset includes $N = 153\,502$ images. Note, that the AUROC is monotonically increasing, while sensitivity, specificity and accuracy exhibit more variation. This is due to the fact that all training processes were optimized for the AUROC. Dashed lines correspond to the non-private training results.

3.2 Diagnostic accuracy is correlated with patient age and sample size for both private and non-private models

Figure 2 shows the difference in classification performance on the UKA-CXR dataset for each diagnosis between the non-private model evaluation and its private counterpart compared to the sample size (that is, the number of available samples with a given label) within our dataset. At an $\epsilon = 7.89$, the largest difference of AUROC between the non-private and privacy-preserving model was observed for congestion (3.82%) and the smallest difference was observed for pleural effusion right (1.55%, see Figure 2). Of note, there is a visible trend (Pearson’s r : 0.44) whereby classes in which the model exhibits good diagnostic performance in the non-private setting also suffer the smallest drop in the private setting. On the other hand, classes that are already difficult to predict in the non-private case deteriorate the most in terms of classification performance with DP (see Supplementary Figure 15). Both non-private (Pearson’s r : 0.57) and private (Pearson’s r : 0.52) diagnostic AUROC exhibit a weak correlation with the number of samples available for each class (see Supplementary Figure 15). However, the drop in AUROC between private and non-private training is not correlated with the sample size (Pearson’s r : 0.06). On the PDAC dataset, patients with a tumor are overrepresented and in the non-private case diagnosed more accurately. Not surprisingly, the classification performance is thus also higher for private trainings except for the most restrictive privacy budget (see Figure 11).

Furthermore, we evaluated our models based on age range and patient sex (Table 1). Additionally, we calculated statistical parity difference for those groups to obtain a measure of fairness (Table 1 and Figure

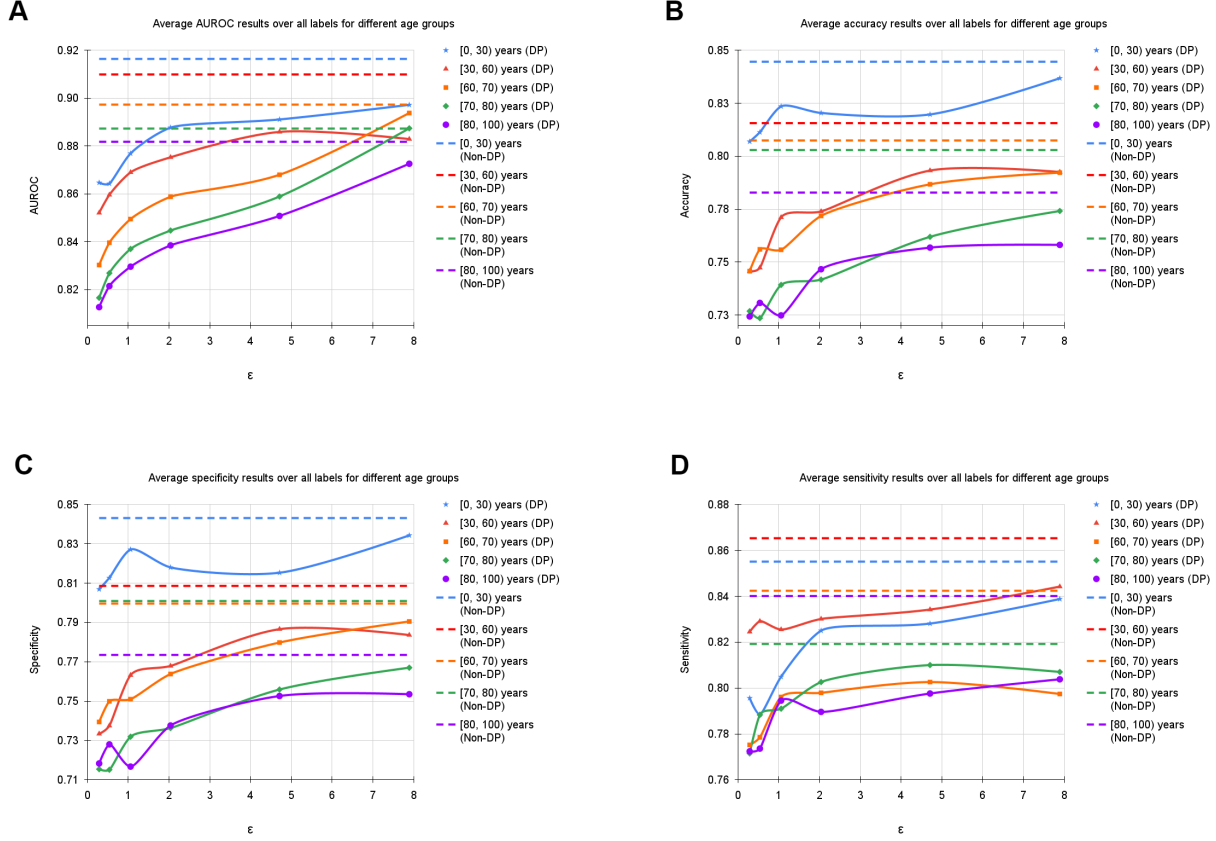


Figure 4: Average results of training with DP with different ε values for $\delta = 6 \cdot 10^{-6}$, separately for samples of different age groups including [0, 30), [30, 60), [60, 70), [70, 80), and [80, 100) years. The curves show the average (A) AUROC, (B) accuracy, (C) specificity, and (D) sensitivity values over all labels, including cardiomegaly, congestion, pleural effusion right, pleural effusion left, pneumonic infiltration right, pneumonic infiltration left, atelectasis right, and atelectasis left tested on $N = 39\,809$ test images. The training dataset includes $N = 153\,502$ images. Dashed lines in corresponding colors correspond to the non-private training results.

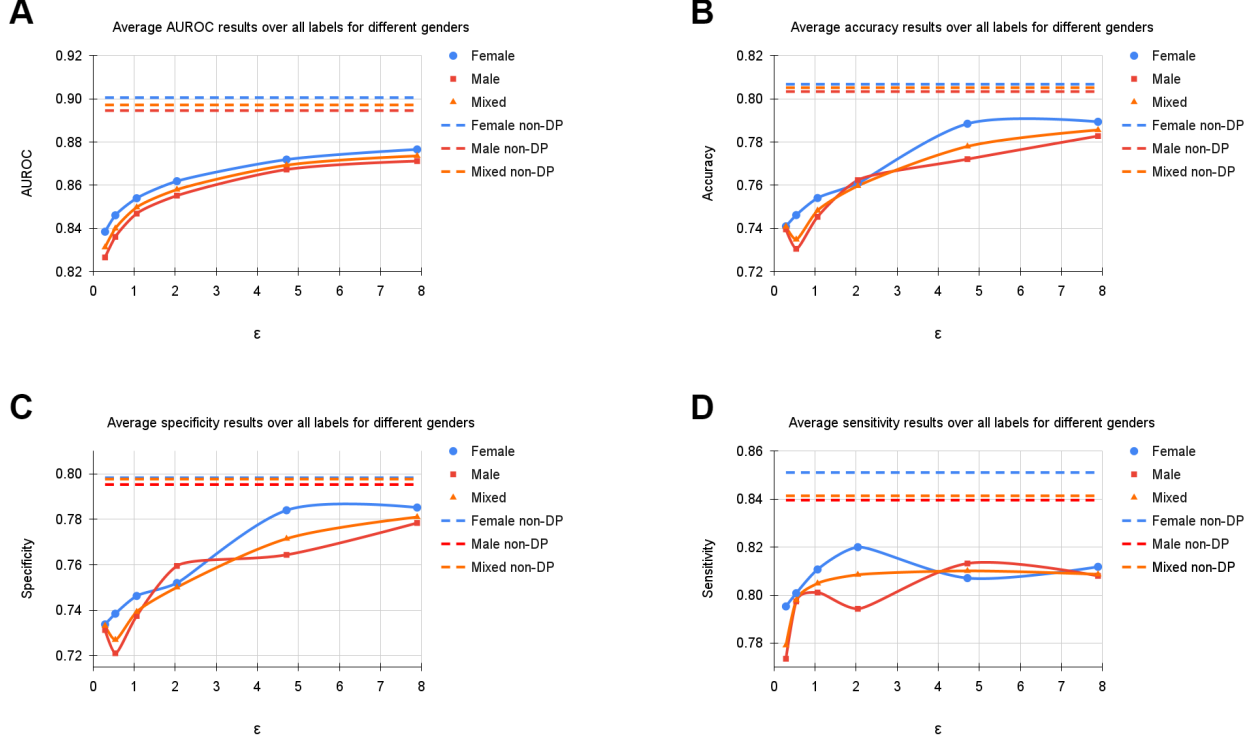


Figure 5: Average results of training with DP with different ε values for $\delta = 6 \cdot 10^{-6}$, separately for female and male samples. The curves show the average (A) AUROC, (B) accuracy, (C) specificity, and (D) sensitivity values over all labels, including cardiomegaly, congestion, pleural effusion right, pleural effusion left, pneumonic infiltration right, pneumonic infiltration left, atelectasis right, and atelectasis left tested on $N = 39\,809$ test images. The training dataset includes $N = 153\,502$ images. Note, that the AUROC is monotonically increasing, while sensitivity, specificity and accuracy exhibit more variation. This is due to the fact that all training processes were optimized for the AUROC. Dashed lines correspond to the non-private training results depicted as upper bounds.

5). On the UKA-CXR dataset all models performed the best on patients younger than 30 years of age. It appears that, the older patients are, the greater the difficulty for the models to predict the labels accurately. Statistical parity difference scores are slightly negative for the age groups between 70 and 80 years and older than 80 years for all models, indicating that the models discriminate slightly against these groups. In addition, while for the aforementioned age groups the discrimination does not change with privacy levels, younger patients become more privileged as privacy increases. This finding indicates that –for models which are most protective of data privacy– young patients benefit the most, despite the group of younger patients being smaller overall. For patient sex, models show slightly better performance for female patients and slightly discriminate against male patients (Table 1). Statistical parity does not appear to correlate (Pearson’s r : 0.13) with privacy levels.

On the PDAC dataset, we observed that, for all levels of privacy including non-private training, classification performance was worse for female patients compared to male patients, who are over-represented in the dataset. However, there is no trend observable between the privacy level and the parity difference. When analysing results of subgroups separated by patient age, we observed similarly to UKA-CXR that in all settings, statistical parity differences are on average better for younger patients compared to older ones. Just as in the UKA-CXR dataset, we found that the more restrictive the privacy budget is set, the stronger the privilege enjoyed by younger patients. We furthermore observed that the control group (i.e. no tumor) has an over-representation of both male patients and young patients, which consequently both exhibit better performance compared to the rest of the cohort. Conversely, female patients as well as older patients, have a

higher chance of misclassification and are more abundant in the tumor group.

4 Discussion

The main contribution of our paper is to analyse the impact of strong objective guarantees of privacy on the fairness enjoyed by specific patient subgroups in the context of AI model training on real-world medical datasets.

Across all levels of privacy protection, training with DP still yielded models exhibiting AUROC scores of 83% at the highest privacy level and 87% at an $\epsilon = 7.89$ on the UKA-CXR dataset. The fact that the model maintained a relatively high AUROC even at $\epsilon = 0.29$ is remarkable, and we are unaware of any prior work to report such a strong level of privacy protection at this level of model accuracy on clinical data. Our results thus exemplify that, through careful choice of architectures and best practices for the training of DP models, the use of model pretraining on a related public dataset, and the availability of sufficient data samples, privately trained models require only very small additional amounts of private information from the training dataset to achieve high diagnostic accuracy on the tasks at hand. For the PDAC dataset, even though private models at $\epsilon = 8.0$ are not significantly inferior compared to non-private counterparts, the effect of the lower amount of training samples is observable at more restrictive privacy budgets. Especially at $\epsilon \leq 1.06$, the negative effect of private training on the discrimination of patients in certain age groups becomes noticeable. This underscores the requirement for larger training datasets, which the objective privacy guarantees of DP can enable through incentivizing data sharing.

Our analysis of the per-diagnosis performance of models that are trained with and without privacy guarantees shows that models discriminate against diagnoses that are underrepresented in the training set in both private and non-private training. This finding is not unusual and several examples can be found in [50]. However, the drop in performance between private and non-private training is uncorrelated to the sample size. Instead, the difficulty of the diagnosis seems to drive the difference in AUROC between the two settings. Concretely, diagnostic performance under privacy constraints suffers the most for those classes, which already have the lowest AUROC in the non-private setting. Conversely, diagnoses that are predicted with the highest AUROC suffer the least when DP is introduced.

Previous works investigating the effect of DP on fairness show that privacy preservation amplifies discrimination [29]. This effect is limited to very low privacy budgets in our study. Our models remain fair despite at the levels of privacy protection typically used for training state-of-the-art models in current literature [25], likely due to our real-life datasets’ large size and/or high quality.

The effects we observed are not limited to within-domain models. Indeed, in a concurrent work, we investigated the effects of DP training on the domain generalizability of diagnostic medical AI models [51]. Our findings revealed that even under extreme privacy conditions, DP-trained models show comparable performance to non-DP models in external domains.

Our analysis of fairness related to patient age showed that older patients are discriminated against both in the non-private and private settings. On UKA-CXR, age-related discrimination remains approximately constant with stronger privacy guarantees. On the other hand, young patients enjoy overall lower model discrimination in the non-private and the private setting. Interestingly, young patients seem to profit more from stronger privacy guarantees, as they enjoy progressively more fairness privilege with increasing privacy protection level. This holds despite the fact that patients under 30 represent the smallest fraction of the UKA-CXR dataset. The privilege of young patients is most likely due to a confounding variable, namely the lower complexity of imaging findings in younger patients due to their improved ability to cooperate during radiograph acquisition, resulting in better discrimination of the pathological finding on a more homogeneous background (i.e., “cleaner”) radiographs which are easier to diagnose overall [35, 52] (see Figure 6). This hypothesis should be validated in cohorts with a larger proportion of young patients, and we intend to expand on this finding in future work. On the PDAC dataset, classification accuracy remains approximately on par between age subgroups except at very restrictive privacy budgets, where older patients begin to suffer discrimination, likely due to the aforementioned imbalance between control and tumor cases and the overall smaller dataset coupled with a lack of pre-training. The analysis of model fairness related to patient sex for UKA-CXR shows that female patients (which –similar to young patients– are an underrepresented group) enjoy a slightly higher diagnostic accuracy than male patients for almost all privacy levels and *vice versa* on

the PDAC dataset. However, effect size differences were found to be small, so that this finding can also be explained by variability between models or by the randomness in the training process. Further investigation is thus required to elucidate the aforementioned effects.

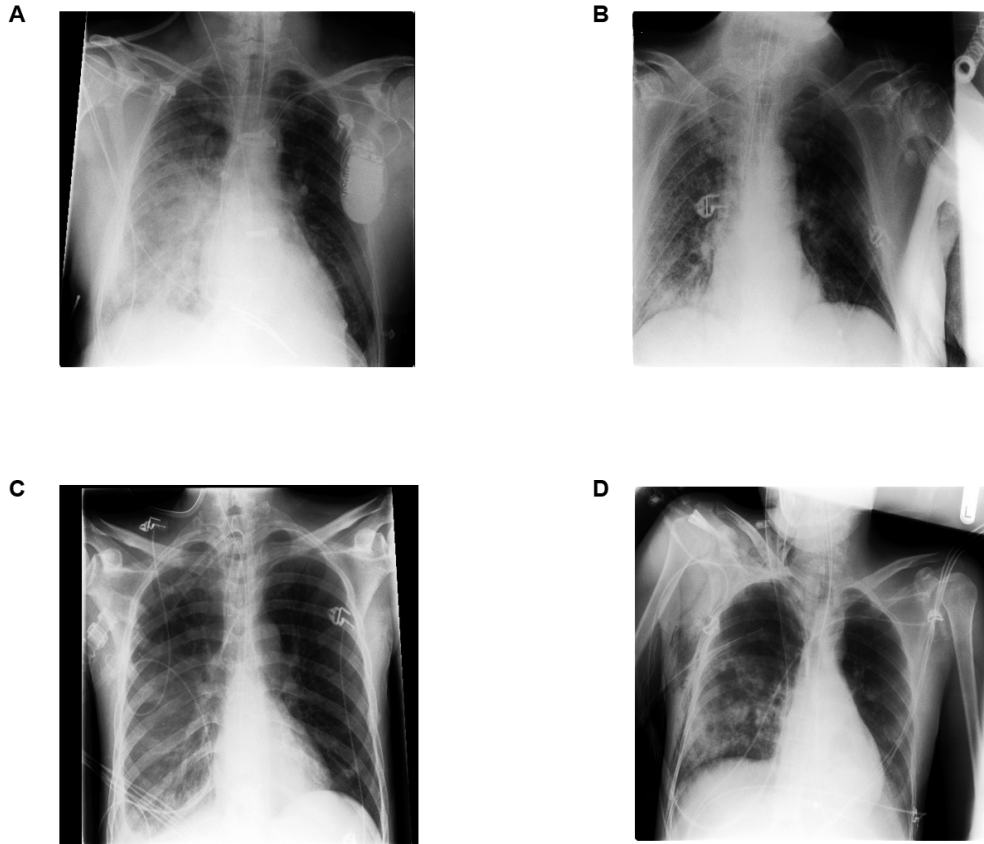


Figure 6: Illustrative radiographs from the UKA-CXR dataset. All examinations share the diagnosis of pneumonic infiltrates on the right patient side (=left image side). However, diagnosis in older patients is often more challenging due to the more frequent presence of comorbidities and less cooperation during image acquisition which results in lower image quality (A) 76-year-old male patient, note the presence of a cardiac pacemaker that projects over part of the left lung. (B) 74-year-old male patient with challenging image acquisition: part of the lower right lung is not properly depicted. (C) 39-year-old male patient, the lungs are well inflated and pneumonic infiltrates can be discerned even though they are less severe. (D) 33-year-old male patient with challenging image acquisition, yet both lungs can be assessed (almost) completely.

Furthermore, there is no final conclusion for which fairness measure is preferable. In our study we focused on the statistical parity difference, however, there are other works proposing other measures. One, which recently received attention, is the underdiagnosis rate of subgroups [53]. We evaluated this for the PDAC dataset and found that in principle it shows the same trends as the statistical parity difference (see Table 10).

In conclusion, we analyzed the usage of privacy-preserving neural network training and its implications on utility and fairness for a relevant diagnostic task on a large real-world dataset. We showed that the utilization of specialized architectures and targeted model pre-training allows for high model accuracy despite stringent privacy guarantees. This enables us to train expert-level diagnostic AI models even with privacy budgets as low as $\epsilon < 1$, which – to our knowledge – has not been shown before, and represents an important step towards the widespread utilization of differentially private models in radiological diagnostic AI applications. Moreover, our findings that the introduction of differential privacy mechanisms to model training does –in most cases– not amplify unfair model bias regarding patient age, sex or comorbidity signifies that –at least in our use case– the resulting models abide by important non-discrimination principles of ethical AI. We are hopeful that our findings will encourage practitioners and clinicians to introduce advanced privacy-preserving

techniques such as differential privacy when training diagnostic AI models.

References

- [1] Dmitrii Usynin, Alexander Ziller, Marcus Makowski, Rickmer Braren, Daniel Rueckert, Ben Glocker, Georgios Kaissis, and Jonathan Passerat-Palmbach. Adversarial interference and its mitigations in privacy-preserving collaborative machine learning. *Nature Machine Intelligence*, 3(9):749–758, 2021.
- [2] Jakub Konečný, H Brendan McMahan, Daniel Ramage, and Peter Richtárik. Federated optimization: Distributed machine learning for on-device intelligence. *arXiv preprint arXiv:1610.02527*, 2016.
- [3] Jakub Konečný, H Brendan McMahan, Felix X Yu, Peter Richtárik, Ananda Theertha Suresh, and Dave Bacon. Federated learning: Strategies for improving communication efficiency. *arXiv preprint arXiv:1610.05492*, 2016.
- [4] Brendan McMahan, Eider Moore, Daniel Ramage, Seth Hampson, and Blaise Agüera y Arcas. Communication-efficient learning of deep networks from decentralized data. In *Artificial intelligence and statistics*, pages 1273–1282. PMLR, 2017.
- [5] Daniel Truhn, Soroosh Tayebi Arasteh, Oliver Lester Saldanha, Gustav Müller-Franzes, Firas Khader, Philip Quirke, Nicholas P West, Richard Gray, Gordon GA Hutchins, Jacqueline A James, et al. Encrypted federated learning for secure decentralized collaboration in cancer image analysis. *medRxiv*, pages 2022–07, 2022.
- [6] Cynthia Dwork, Aaron Roth, et al. The algorithmic foundations of differential privacy. *Found. Trends Theor. Comput. Sci.*, 9(3-4):211–407, 2014.
- [7] Franziska Boenisch, Adam Dziedzic, Roei Schuster, Ali Shahin Shamsabadi, Ilia Shumailov, and Nicolas Papernot. When the curious abandon honesty: Federated learning is not private. *arXiv preprint arXiv:2112.02918*, 2021.
- [8] Liam Fowl, Jonas Geiping, Wojtek Czaja, Micah Goldblum, and Tom Goldstein. Robbing the fed: Directly obtaining private data in federated learning with modified models. *arXiv preprint arXiv:2110.13057*, 2021.
- [9] Kuan-Chieh Wang, Yan Fu, Ke Li, Ashish Khisti, Richard Zemel, and Alireza Makhzani. Variational model inversion attacks. *Advances in Neural Information Processing Systems*, 34:9706–9719, 2021.
- [10] Niv Haim, Gal Vardi, Gilad Yehudai, Ohad Shamir, and Michal Irani. Reconstructing training data from trained neural networks. *Advances in Neural Information Processing Systems*, 35:22911–22924, 2022.
- [11] Nicholas Carlini, Jamie Hayes, Milad Nasr, Matthew Jagielski, Vikash Sehwal, Florian Tramèr, Borja Balle, Daphne Ippolito, and Eric Wallace. Extracting training data from diffusion models. *arXiv preprint arXiv:2301.13188*, 2023.
- [12] U.S. Food and Drug Administration. Artificial intelligence and machine learning (ai/ml)-enabled medical devices. <https://www.fda.gov/medical-devices/software-medical-device-samd/artificial-intelligence-and-machine-learning-aiml-enabled-medical-devices>.
- [13] Larry Wasserman and Shuheng Zhou. A statistical framework for differential privacy. *Journal of the American Statistical Association*, 105(489):375–389, 2010.
- [14] Jinshuo Dong, Aaron Roth, and Weijie J Su. Gaussian differential privacy. *Journal of the Royal Statistical Society Series B: Statistical Methodology*, 84(1):3–37, 2022.
- [15] Georgios Kaissis, Jamie Hayes, Alexander Ziller, and Daniel Rueckert. Bounding data reconstruction attacks with the hypothesis testing interpretation of differential privacy. *arXiv preprint arXiv:2307.03928*, 2023.

- [16] Milad Nasr, Jamie Hayes, Thomas Steinke, Borja Balle, Florian Tramèr, Matthew Jagielski, Nicholas Carlini, and Andreas Terzis. Tight auditing of differentially private machine learning. *arXiv preprint arXiv:2302.07956*, 2023.
- [17] Georgios Kaissis, Alexander Ziller, Jonathan Passerat-Palmbach, Théo Ryffel, Dmitrii Usynin, Andrew Trask, Ionésio Lima Jr, Jason Mancuso, Friederike Jungmann, Marc-Matthias Steinborn, et al. End-to-end privacy preserving deep learning on multi-institutional medical imaging. *Nature Machine Intelligence*, 3(6):473–484, 2021.
- [18] Jamie Hayes, Saeed Mahloujifar, and Borja Balle. Bounding training data reconstruction in dp-sgd. *arXiv preprint arXiv:2302.07225*, 2023.
- [19] Borja Balle, Giovanni Cherubin, and Jamie Hayes. Reconstructing training data with informed adversaries. In *2022 IEEE Symposium on Security and Privacy (SP)*, pages 1138–1156. IEEE, 2022.
- [20] Aloni Cohen and Kobbi Nissim. Towards formalizing the gdpr’s notion of singling out. *Proceedings of the National Academy of Sciences*, 117(15):8344–8352, 2020.
- [21] Aloni Cohen. Attacks on deidentification’s defenses. In *31st USENIX Security Symposium (USENIX Security 22)*, pages 1469–1486, 2022.
- [22] Martin Abadi, Andy Chu, Ian Goodfellow, H Brendan McMahan, Ilya Mironov, Kunal Talwar, and Li Zhang. Deep learning with differential privacy. In *Proceedings of the 2016 ACM SIGSAC conference on computer and communications security*, pages 308–318, 2016.
- [23] Ali Hatamizadeh, Hongxu Yin, Pavlo Molchanov, Andriy Myronenko, Wenqi Li, Prerna Dogra, Andrew Feng, Mona G Flores, Jan Kautz, Daguang Xu, et al. Do gradient inversion attacks make federated learning unsafe? *IEEE Transactions on Medical Imaging*, 2023.
- [24] Cynthia Dwork. A firm foundation for private data analysis. *Communications of the ACM*, 54(1):86–95, 2011.
- [25] Soham De, Leonard Berrada, Jamie Hayes, Samuel L Smith, and Borja Balle. Unlocking high-accuracy differentially private image classification through scale. *arXiv preprint arXiv:2204.13650*, 2022.
- [26] Alexey Kurakin, Steve Chien, Shuang Song, Roxana Geambasu, Andreas Terzis, and Abhradeep Thakurta. Toward training at imagenet scale with differential privacy. *arXiv preprint arXiv:2201.12328*, 2022.
- [27] Cuong Tran, Ferdinando Fioretto, Pascal Van Hentenryck, and Zhiyan Yao. Decision making with differential privacy under a fairness lens. In *IJCAI*, pages 560–566, 2021.
- [28] Rachel Cummings, Varun Gupta, Dhamma Kimpara, and Jamie Morgenstern. On the compatibility of privacy and fairness. In *Adjunct Publication of the 27th Conference on User Modeling, Adaptation and Personalization*, pages 309–315, 2019.
- [29] Tom Farrand, Fatemehsadat Mireshghallah, Sahib Singh, and Andrew Trask. Neither private nor fair: Impact of data imbalance on utility and fairness in differential privacy. In *Proceedings of the 2020 workshop on privacy-preserving machine learning in practice*, pages 15–19, 2020.
- [30] Eugene Bagdasaryan, Omid Poursaeed, and Vitaly Shmatikov. Differential privacy has disparate impact on model accuracy. *Advances in neural information processing systems*, 32, 2019.
- [31] Kai Packhäuser, Sebastian Gündel, Nicolas Münster, Christopher Syben, Vincent Christlein, and Andreas Maier. Deep learning-based patient re-identification is able to exploit the biometric nature of medical chest x-ray data. *Scientific Reports*, 12(1):14851, 2022.
- [32] Arvind Narayanan and Vitaly Shmatikov. Robust de-anonymization of large sparse datasets. In *2008 IEEE Symposium on Security and Privacy (sp 2008)*, pages 111–125. IEEE, 2008.

- [33] Wenqi Li, Fausto Milletari, Daguang Xu, Nicola Rieke, Jonny Hancox, Wentao Zhu, Maximilian Baust, Yan Cheng, Sébastien Ourselin, M Jorge Cardoso, et al. Privacy-preserving federated brain tumour segmentation. In *Machine Learning in Medical Imaging: 10th International Workshop, MLMI 2019, Held in Conjunction with MICCAI 2019, Shenzhen, China, October 13, 2019, Proceedings 10*, pages 133–141. Springer, 2019.
- [34] Joceline Ziegler, Bjarne Pfitzner, Heinrich Schulz, Axel Saalbach, and Bert Arnrich. Defending against reconstruction attacks through differentially private federated learning for classification of heterogeneous chest x-ray data. *Sensors*, 22(14):5195, 2022.
- [35] Firas Khader, Tianyu Han, Gustav Müller-Franzes, Luisa Huck, Philipp Schad, Sebastian Keil, Emona Barzakova, Maximilian Schulze-Hagen, Federico Pedersoli, Volkmar Schulz, et al. Artificial intelligence for clinical interpretation of bedside chest radiographs. *Radiology*, page 220510, 2022.
- [36] Soroosh Tayebi Arasteh, Peter Isfort, Marwin Saehn, Gustav Mueller-Franzes, Firas Khader, Jakob Nikolas Kather, Christiane Kuhl, Sven Nebelung, and Daniel Truhn. Collaborative training of medical artificial intelligence models with non-uniform labels. *Scientific Reports*, 13(1):6046, 2023.
- [37] Alistair EW Johnson, Tom J Pollard, Seth J Berkowitz, Nathaniel R Greenbaum, Matthew P Lungren, Chih-ying Deng, Roger G Mark, and Steven Horng. Mimic-cxr, a de-identified publicly available database of chest radiographs with free-text reports. *Scientific data*, 6(1):317, 2019.
- [38] Helena Klause, Alexander Ziller, Daniel Rueckert, Kerstin Hammernik, and Georgios Kaissis. Differentially private training of residual networks with scale normalisation. *Theory and Practice of Differential Privacy Workshop, ICML*, 2022.
- [39] Jiancheng Yang, Xiaoyang Huang, Yi He, Jingwei Xu, Canqian Yang, Guozheng Xu, and Bingbing Ni. Reinventing 2d convolutions for 3d images. *IEEE Journal of Biomedical and Health Informatics*, 25(8):3009–3018, 2021.
- [40] Kaiming He, Xiangyu Zhang, Shaoqing Ren, and Jian Sun. Deep residual learning for image recognition. In *Proceedings of the IEEE conference on computer vision and pattern recognition*, pages 770–778, 2016.
- [41] Sergey Ioffe and Christian Szegedy. Batch normalization: Accelerating deep network training by reducing internal covariate shift. In *International conference on machine learning*, pages 448–456. pmlr, 2015.
- [42] Yuxin Wu and Kaiming He. Group normalization. In *Proceedings of the European conference on computer vision (ECCV)*, pages 3–19, 2018.
- [43] Alistair EW Johnson, Tom J Pollard, Nathaniel R Greenbaum, Matthew P Lungren, Chih-ying Deng, Yifan Peng, Zhiyong Lu, Roger G Mark, Seth J Berkowitz, and Steven Horng. Mimic-cxr-jpg, a large publicly available database of labeled chest radiographs. *arXiv preprint arXiv:1901.07042*, 2019.
- [44] Abien Fred Agarap. Deep learning using rectified linear units (relu). *arXiv preprint arXiv:1803.08375*, 2018.
- [45] Timothy Dozat. Incorporating nesterov momentum into adam. 2016.
- [46] Diganta Misra. Mish: A self regularized non-monotonic activation function. *arXiv preprint arXiv:1908.08681*, 2019.
- [47] Frank Konietzschke and Markus Pauly. Bootstrapping and permuting paired t-test type statistics. *Statistics and Computing*, 24:283–296, 2014.
- [48] Ilker Unal. Defining an optimal cut-point value in roc analysis: an alternative approach. *Computational and mathematical methods in medicine*, 2017, 2017.
- [49] Toon Calders and Sicco Verwer. Three naive bayes approaches for discrimination-free classification. *Data mining and knowledge discovery*, 21:277–292, 2010.

- [50] Ninareh Mehrabi, Fred Morstatter, Nripsuta Saxena, Kristina Lerman, and Aram Galstyan. A survey on bias and fairness in machine learning. *ACM Computing Surveys (CSUR)*, 54(6):1–35, 2021.
- [51] Soroosh Tayebi Arasteh, Mahshad Lotfinia, Teresa Nolte, Marwin Saehn, Peter Isfort, Christiane Kuhl, Sven Nebelung, Georgios Kaissis, and Daniel Truhn. Preserving privacy in domain transfer of medical ai models comes at no performance costs: The integral role of differential privacy. *arXiv preprint arXiv:2306.06503*, 2023.
- [52] Joy T Wu, Ken CL Wong, Yaniv Gur, Nadeem Ansari, Alexandros Karargyris, Arjun Sharma, Michael Morris, Babak Saboury, Hassan Ahmad, Orest Boyko, et al. Comparison of chest radiograph interpretations by artificial intelligence algorithm vs radiology residents. *JAMA network open*, 3(10):e2022779–e2022779, 2020.
- [53] Laleh Seyyed-Kalantari, Haoran Zhang, Matthew BA McDermott, Irene Y Chen, and Marzyeh Ghassemi. Underdiagnosis bias of artificial intelligence algorithms applied to chest radiographs in under-served patient populations. *Nature medicine*, 27(12):2176–2182, 2021.
- [54] Ashkan Yousefpour, Igor Shilov, Alexandre Sablayrolles, Davide Testuggine, Karthik Prasad, Mani Malek, John Nguyen, Sayan Ghosh, Akash Bharadwaj, Jessica Zhao, Graham Cormode, and Ilya Mironov. Opacus: User-friendly differential privacy library in pytorch, 2021.
- [55] Coen de Vente, Koenraad A. Vermeer, Nicolas Jaccard, He Wang, Hongyi Sun, Firas Khader, Daniel Truhn, Temirgali Aimyshev, Yerkebulan Zhanibekuly, Tien-Dung Le, Adrian Galdran, Miguel Ángel González Ballester, Gustavo Carneiro, Devika R G, Hrishikesh P S, Densen Puthussery, Hong Liu, Zekang Yang, Satoshi Kondo, Satoshi Kasai, Edward Wang, Ashritha Durvasula, Jónathan Heras, Miguel Ángel Zapata, Teresa Araújo, Guilherme Aresta, Hrvoje Bogunović, Mustafa Arikian, Yeong Chan Lee, Hyun Bin Cho, Yoon Ho Choi, Abdul Qayyum, Imran Razzak, Bram van Ginneken, Hans G. Lemij, and Clara I. Sánchez. Airops: Artificial intelligence for robust glaucoma screening challenge. *arXiv preprint arXiv:2302.01738*, 2023.
- [56] Mingxing Tan and Quoc Le. Efficientnet: Rethinking model scaling for convolutional neural networks. In *Proceedings of the 36th International Conference on Machine Learning*, pages 6105–6114, 2019.
- [57] Gao Huang, Zhuang Liu, Laurens van der Maaten, and Kilian Q. Weinberger. Densely connected convolutional networks. In *Proceedings of the IEEE Conference on Computer Vision and Pattern Recognition (CVPR)*, pages 4700–4708, 2017.
- [58] Firas Khader, Christoph Haarbuerger, Jörg-Christian Kirr, Marcel Menke, Jakob Nikolas Kather, Johannes Stegmaier, Christiane Kuhl, Sven Nebelung, and Daniel Truhn. Elevating fundoscopic evaluation to expert level - automatic glaucoma detection using data from the airops challenge. In *2022 IEEE International Symposium on Biomedical Imaging Challenges (ISBIC)*, pages 1–4, 2022.
- [59] Ahmed Al-Mahrooqi, Dmitrii Medvedev, Rand Muhtaseb, and Mohammad Yaqub. Gardnet: Robust multi-view network for glaucoma classification in color fundus images. In Bhavna Antony, Huazhu Fu, Cecilia S. Lee, Tom MacGillivray, Yanwu Xu, and Yalin Zheng, editors, *Ophthalmic Medical Image Analysis*, pages 152–161, Cham, 2022. Springer International Publishing.
- [60] Jia Deng, Wei Dong, Richard Socher, Li-Jia Li, Kai Li, and Li Fei-Fei. Imagenet: A large-scale hierarchical image database. In *2009 IEEE Conference on Computer Vision and Pattern Recognition*, pages 248–255, 2009.

Ethics Statement

The experiments were performed in accordance with relevant guidelines and regulations. Approval for UKA-CXR by the Ethical Committee of the Medical Faculty of RWTH Aachen University has been granted for this retrospective study (Reference No. EK 028/19). The institutional review board did not require informed consent from subjects and/or their legal guardian(s). The study was conducted in accordance with

the Declaration of Helsinki, and the protocol for the PDAC dataset was approved by the Ethics Committee of Klinikum Rechts der Isar (Protocol Number 180/17S).

Acknowledgements

STA is funded and supported by the Radiological Cooperative Network (RACOON) under the German Federal Ministry of Education and Research (BMBF) grant number 01KX2021. The funders played no role in the design or execution of the study. This work has been funded by the German Federal Ministry of Education and Research and the Bavarian State Ministry for Science and the Arts. The authors of this work take full responsibility for its content.

Author Contributions Statement

The formal analysis was conducted by STA, AZ, DT, and GK. The original draft was written by STA and AZ and edited by DT and GK. The experiments as well as the software development for UKA-CXR were performed by STA and for PDAC by AZ. Statistical analyses were performed by AZ and STA. DT and GK provided clinical and technical expertise. All authors read the manuscript and contributed to the interpretation of the results and agreed to the submission of this paper.

Competing Interests

The authors declare no competing interests.

Code and Data Availability

All source codes used for UKA-CXR for training and evaluation of the deep neural networks, differential privacy, data augmentation, image analysis, and preprocessing are publicly available at https://github.com/tayebiarasteh/DP_CXR. All code for the experiments was developed in Python 3.9 using the PyTorch 2.0 framework. The DP code was developed using Opacus 1.4.0 [54]. Considering the utilization of equivalent computational resources, the time taken for the DP training to converge was approximately 10 times longer, in terms of total training time, than that required for the non-DP training with a similar network architecture. All code for the analyses on the PDAC dataset are available at <https://github.com/TUM-AIMED/2.5DAttention>.

The UKA-CXR data is not publicly accessible as it is internal data of patients of University Hospital RWTH Aachen in Aachen, Germany. The PDAC dataset is an in-house dataset at Klinikum Rechts der Isar, Munich, Germany. Data access for both datasets can be granted upon reasonable request to the corresponding author. The Rotterdam EyePACS AIROGS funduscopy [55] training data are available on Zenodo via <https://zenodo.org/record/5793241>.

Hardware

The hardware used in our experiments were Intel CPUs with 18 cores and 32 GB RAM and Nvidia RTX 6000 GPU with 24 GB of VRAM.

Appendices

UKA-CXR																
		Total	Male		Female		[0,30)		[30,60)		[60,70)		[70,80)		[80,100)	
Train	N	153 502	100 659		52 843		4 279		42 340		36 882		48 864		21 137	
Test	N	39 809	25 360		14 449		1 165		10 291		10 025		12 958		5 370	
	Cardiomegaly	18 616	12 868		5 748		334		3 853		4 714		6 837		2 876	
	Congestion	3 275	2 206		1 069		50		817		906		991		510	
	Pl. Eff. R.	3 275	2 090		1 185		52		709		847		1 248		419	
	Pl. Eff. L.	2 602	1 636		966		70		589		632		894		417	
	Pn. Inf. R.	4 847	3 374		1 473		184		1 322		1 367		1 361		612	
	Pn. Inf. L.	3 562	2 381		1 181		143		1 087		949		959		423	
	Atel. R.	3 920	2 571		1 349		127		1 010		1 056		1 272		454	
	Atel. L.	3 166	2 010		1 156		119		867		774		961		444	
		ε	μ	σ	μ	σ	μ	σ	μ	σ	μ	σ	μ	σ	μ	σ
AUROC	0.29		83.13	3.9	82.66	3.9	83.85	4.0	86.47	3.5	85.21	3.9	83.03	3.6	81.66	4.5
	0.54		84.00	3.8	83.61	3.8	84.61	3.9	86.43	3.1	85.96	3.7	83.96	3.5	82.69	4.5
	1.06		84.98	3.9	84.69	3.9	85.40	4.0	87.69	3.2	86.90	3.7	84.95	3.8	83.70	4.5
	2.04		85.80	3.9	85.52	3.9	86.19	3.9	88.77	3.3	87.53	3.8	85.88	3.8	84.47	4.4
	4.71		86.93	4.0	86.73	4.1	87.19	4.0	89.11	3.3	88.59	3.9	86.80	3.7	85.89	4.7
	7.89		87.36	4.1	87.12	4.2	87.66	4.1	89.72	4.1	88.97	3.9	87.26	3.9	86.30	4.7
	∞		89.71	3.8	89.46	3.9	90.06	3.8	91.64	3.5	90.99	3.4	89.73	3.8	88.73	4.4
PtD	0.29				-1.40	0.22	+1.40	0.22	+7.05	0.18	+0.98	0.73	+0.97	1.75	-1.73	0.36
	0.54				-1.56	0.10	+1.56	0.10	+7.20	0.21	+0.80	0.52	+1.95	0.48	-2.65	0.31
	1.06				-0.87	0.73	+0.87	0.73	+7.35	0.51	+2.56	0.67	+0.49	0.23	-1.92	0.78
	2.04				+0.15	0.42	-0.15	0.42	+6.12	0.92	+1.80	0.39	+1.50	0.00	-2.80	0.30
	4.71				-1.63	0.31	+1.63	0.31	+4.37	0.18	+2.15	0.70	+1.26	1.38	-2.27	0.50
	7.89				-0.66	0.75	+0.66	0.75	+5.53	0.92	+1.27	0.04	+1.21	0.22	-1.33	0.06
	∞				-0.34	0.47	+0.34	0.47	+4.00	0.60	+1.32	0.65	+0.21	0.66	-0.43	0.95
PDAC																
		Total	Male		Female		Youngest 25%		Second 25%		Third 25%		Oldest 25%			
Train	N	975	552		423		231		290		228		226			
Test	N	325	197		127		86		85		79		75			
	Tumour	173	95		77		23		48		54		48			
	Control	152	102		50		63		37		25		27			
		ε	μ	σ	μ	σ	μ	σ	μ	σ	μ	σ	μ	σ	μ	σ
AUROC	0.29		86.84	4.0	88.11	4.6	85.47	2.5	87.92	9.1	85.87	3.0	84.44	1.2	89.15	7.2
	0.54		92.60	1.3	93.62	1.5	91.00	0.9	93.77	3.2	91.97	1.2	90.05	0.4	95.63	2.3
	1.06		95.58	0.9	96.70	0.9	93.52	1.3	96.57	1.6	94.84	1.3	93.83	1.1	98.43	0.9
	2.04		97.49	0.4	98.50	0.3	95.36	0.9	97.98	0.9	96.90	0.8	97.06	0.9	99.36	0.6
	4.71		98.31	0.2	99.19	0.1	96.38	0.7	98.48	0.3	97.84	0.2	98.30	0.4	99.97	0.0
	5.0		98.33	0.2	99.20	0.1	96.41	0.7	98.48	0.4	97.86	0.1	98.37	0.4	100.00	0.0
	6.0		98.39	0.3	99.22	0.1	96.55	0.8	98.57	0.3	97.84	0.2	98.35	0.5	100.00	0.0
	7.0		98.41	0.3	99.22	0.1	96.60	0.8	98.62	0.3	97.88	0.1	98.25	0.5	100.00	0.0
	8.0		99.28	0.7	99.77	0.3	98.13	1.6	99.59	0.7	99.23	1.2	98.37	0.9	100.00	0.0
	∞		99.70	0.2	99.97	0.1	99.01	0.6	99.98	0.0	99.94	0.1	98.47	0.9	100.00	0.0
PtD	0.29				+3.27	5.38	-3.27	5.38	+9.03	1.32	+1.87	2.12	-9.54	4.33	-2.04	4.74
	0.54				+1.02	0.76	-1.02	0.76	+3.17	0.54	+0.34	1.44	-7.02	4.39	+3.42	3.28
	1.06				+1.29	1.27	-1.29	1.27	-0.18	3.85	+0.20	1.66	-3.58	3.53	+3.69	2.83
	2.04				+3.00	0.78	-3.00	0.78	-1.97	0.65	-3.16	2.47	+1.55	0.62	+4.00	3.47
	4.71				+4.58	1.33	-4.58	1.33	-3.29	1.23	-2.34	1.20	+1.47	1.46	+4.62	1.46
	5.0				+4.85	1.37	-4.85	1.37	-2.62	0.82	-2.73	1.16	+1.61	0.87	+4.18	1.90
	6.0				+4.41	0.53	-4.41	0.53	-2.10	2.06	-2.20	0.64	+1.05	2.10	+3.60	1.14
	7.0				+3.19	1.27	-3.19	1.27	-1.99	2.97	-3.68	1.21	+1.20	2.31	+4.93	2.02
	8.0				+3.28	2.61	-3.28	2.61	-2.45	1.51	-1.45	2.28	+1.58	2.44	+2.62	1.61
	∞				+2.81	2.38	-2.81	2.38	-1.21	1.59	-0.18	1.16	-0.33	1.71	+1.87	1.22

Table 1: **Summary of dataset statistics and results.** Diagnostic performance of patient sugroups for the UKA-CXR and PDAC datasets. We report the number of cases over subgroups and labels. All values refer to the test set. Total denotes the results on the entire test set. AUROC denotes the area under the receiver-operator curve. PtD is the statistical parity difference of each subgroup. μ are mean values, σ shows the standard deviation. All results are in percent.

A Additional remarks on privacy-utility trade-off

A.1 Varying model architectures

In addition to the ResNet9-architecture reported in the main manuscript, we additionally used three more architectures: An EfficientNet B0, with 4 017 796 parameters, adhering to the original implementation proposed by Tan et al. [56], with the sole exception of replacing all batch normalization layers with group normalization; DenseNet121, with 6 962 056 parameters, following the original design put forth by Huang et al. [57], again with the exclusive modification of substituting batch normalization layers with group normalization; and ResNet18, with 11 180 616 parameters, following the original blueprint developed by He et al. [40], with the unique alteration of replacing batch normalization layers with group normalization. All three models displayed a trend consistent with the utility penalties we observed for ResNet9 in both DP and non-DP training. Compare also Figure 10.

A.2 Further datasets

To prevent domain-specific bias in our results, we employed the Artificial Intelligence for Robust Glaucoma Screening (AIROGS) dataset [55]. This dataset comprises 101 354 RGB ocular fundus images from approximately 60 000 patients of diverse ethnicities, aimed at detecting the presence of referable glaucoma. We allocated 80% of the patients—both with and without glaucoma—to the training set, reserving the remaining 20% for the test set. Image pre-processing involved cropping and other schemes as detailed in [58] and [59]. The images were resized to a dimension of $3 \times 224 \times 224$, with 3 representing the number of channels. We adopted the same EfficientNet B0 network architecture, with identical DP and non-DP training parameters as described earlier, with the same $\delta = 6 \cdot 10^{-6}$. The network was pre-trained on the ImageNet [60] dataset. Figure 16 shows a similar trend as our observations on chest radiographs regarding the privacy-utility trade-off.

B Tables

C Figures

	Training Set		Test Set		All	
	N	percentage	N	percentage	N	percentage
Total	153,502		39,809		193,311	
Female	52,843	(34.42%)	14,449	(36.30%)	67,292	(34.81%)
Male	100,659	(65.58%)	25,360	(63.70%)	126,019	(65.19%)
Aged [0, 30)	4,279	(2.79%)	1,165	(2.93%)	5,444	(2.82%)
Aged [30, 60)	42,340	(27.58%)	10,291	(25.85%)	52,631	(27.23%)
Aged [60, 70)	36,882	(24.03%)	10,025	(25.18%)	46,907	(24.27%)
Aged [70, 80)	48,864	(31.83%)	12,958	(32.55%)	61,822	(31.98%)
Aged [80, 100)	21,137	(13.77%)	5,370	(13.49%)	26,507	(13.71%)
Cardiomegaly	71,732	(46.72%)	18,616	(46.75%)	90,348	(46.74%)
Congestion	13,096	(8.53%)	3,275	(8.22%)	16,371	(8.47%)
Pleural effusion right	12,334	(8.03%)	3,275	(8.22%)	15,609	(8.07%)
Pleural effusion left	9,969	(6.49%)	2,602	(6.53%)	12,571	(6.50%)
Pneumonic infiltration right	17,666	(11.51%)	4,847	(12.17%)	22,513	(11.64%)
Pneumonic infiltration left	12,431	(8.10%)	3,562	(8.94%)	15,993	(8.27%)
Atelectasis right	14,841	(9.67%)	3,920	(9.84%)	18,761	(9.71%)
Atelectasis left	11,916	(7.76%)	3,166	(7.95%)	15,082	(7.80%)
	Age Training Set		Age Test Set		Age All	
	Mean	StD	Mean	StD	Mean	StD
Total	66	15	66	15	66	15
Female	66	15	66	16	66	15
Male	65	14	66	14	65	14
Aged [0, 30)	21	8	21	8	21	8
Aged [30, 60)	50	8	51	8	51	8
Aged [60, 70)	65	3	65	3	65	3
Aged [70, 80)	75	3	75	3	75	3
Aged [80, 100)	84	3	84	3	84	3

Table 2: Statistics over subgroups of the UKA-CXR dataset used in this study. The upper part of the table shows the number of samples in each group and their relative share in training and test set, as well as the complete dataset. The lower part shows the mean and standard deviation of the age in the subgroups again over training and test set as well as the complete dataset.

	AUROC	Accuracy	Specificity	Sensitivity
Cardiomegaly	0.84 \pm 0.00	0.75 \pm 0.00	0.71 \pm 0.02	0.79 \pm 0.02
Congestion	0.85 \pm 0.00	0.75 \pm 0.02	0.75 \pm 0.02	0.79 \pm 0.02
Pleural Effusion Right	0.94 \pm 0.00	0.83 \pm 0.01	0.83 \pm 0.02	0.91 \pm 0.02
Pleural Effusion Left	0.92 \pm 0.00	0.83 \pm 0.02	0.83 \pm 0.02	0.86 \pm 0.02
Pneumonic Infiltration Right	0.93 \pm 0.00	0.85 \pm 0.02	0.85 \pm 0.02	0.86 \pm 0.02
Pneumonic Infiltration Left	0.94 \pm 0.00	0.86 \pm 0.01	0.86 \pm 0.02	0.87 \pm 0.02
Atelectasis Right	0.89 \pm 0.00	0.78 \pm 0.01	0.78 \pm 0.01	0.84 \pm 0.02
Atelectasis Left	0.87 \pm 0.00	0.78 \pm 0.01	0.78 \pm 0.02	0.81 \pm 0.02
Average	0.90 \pm 0.04	0.81 \pm 0.04	0.80 \pm 0.05	0.84 \pm 0.04

Table 3: Detailed evaluation results of training without DP. The results show the average and individual area under the receiver-operator-characteristic curve (AUROC), accuracy, specificity, and sensitivity values for each label tested on $n = 39,809$ test images. The training dataset includes $n = 153,502$ images.

	AUROC	Accuracy	Specificity	Sensitivity
Cardiomegaly	0.82 ± 0.00	0.73 ± 0.00	0.71 ± 0.02	0.76 ± 0.02
Congestion	0.81 ± 0.00	0.72 ± 0.02	0.71 ± 0.03	0.76 ± 0.03
Pleural Effusion Right	0.92 ± 0.00	0.82 ± 0.01	0.82 ± 0.01	0.88 ± 0.01
Pleural Effusion Left	0.89 ± 0.00	0.79 ± 0.02	0.79 ± 0.02	0.84 ± 0.02
Pneumonic Infiltration Right	0.91 ± 0.00	0.84 ± 0.01	0.83 ± 0.02	0.81 ± 0.02
Pneumonic Infiltration Left	0.91 ± 0.00	0.84 ± 0.01	0.84 ± 0.01	0.83 ± 0.01
Atelectasis Right	0.87 ± 0.00	0.78 ± 0.01	0.77 ± 0.01	0.81 ± 0.01
Atelectasis Left	0.85 ± 0.00	0.76 ± 0.02	0.76 ± 0.02	0.79 ± 0.02
Average	0.87 ± 0.04	0.79 ± 0.04	0.78 ± 0.05	0.81 ± 0.04

Table 4: Detailed evaluation results of DP training with $\varepsilon = 7.89$, $\delta = 6 \cdot 10^{-6}$. The results show the average and individual AUROC, accuracy, specificity, and sensitivity values for each label tested on $n = 39,809$ test images. The training dataset includes $n = 153,502$ images.

	AUROC	Accuracy	Specificity	Sensitivity
Cardiomegaly	0.81 ± 0.00	0.73 ± 0.00	0.70 ± 0.01	0.77 ± 0.01
Congestion	0.81 ± 0.00	0.71 ± 0.02	0.70 ± 0.02	0.77 ± 0.02
Pleural Effusion Right	0.92 ± 0.00	0.82 ± 0.01	0.81 ± 0.01	0.87 ± 0.01
Pleural Effusion Left	0.89 ± 0.00	0.80 ± 0.01	0.80 ± 0.02	0.81 ± 0.02
Pneumonic Infiltration Right	0.90 ± 0.00	0.81 ± 0.01	0.81 ± 0.01	0.82 ± 0.01
Pneumonic Infiltration Left	0.91 ± 0.00	0.82 ± 0.01	0.82 ± 0.01	0.85 ± 0.02
Atelectasis Right	0.86 ± 0.00	0.76 ± 0.01	0.75 ± 0.02	0.83 ± 0.02
Atelectasis Left	0.85 ± 0.00	0.78 ± 0.02	0.78 ± 0.03	0.76 ± 0.03
Average	0.87 ± 0.04	0.78 ± 0.04	0.77 ± 0.05	0.81 ± 0.04

Table 5: Detailed evaluation results of DP training with $\varepsilon = 4.71$, $\delta = 6 \cdot 10^{-6}$. The results show the average and individual AUROC, accuracy, specificity, and sensitivity values for each label tested on $n = 39,809$ test images. The training dataset includes $n = 153,502$ images.

	AUROC	Accuracy	Specificity	Sensitivity
Cardiomegaly	0.81 ± 0.00	0.73 ± 0.00	0.68 ± 0.02	0.78 ± 0.02
Congestion	0.80 ± 0.00	0.70 ± 0.02	0.69 ± 0.03	0.76 ± 0.03
Pleural Effusion Right	0.90 ± 0.00	0.80 ± 0.01	0.79 ± 0.01	0.86 ± 0.01
Pleural Effusion Left	0.87 ± 0.00	0.75 ± 0.02	0.74 ± 0.02	0.84 ± 0.02
Pneumonic Infiltration Right	0.90 ± 0.00	0.80 ± 0.01	0.80 ± 0.02	0.83 ± 0.02
Pneumonic Infiltration Left	0.90 ± 0.00	0.83 ± 0.01	0.83 ± 0.02	0.81 ± 0.02
Atelectasis Right	0.85 ± 0.00	0.74 ± 0.02	0.73 ± 0.02	0.82 ± 0.02
Atelectasis Left	0.83 ± 0.00	0.73 ± 0.03	0.73 ± 0.03	0.77 ± 0.03
Average	0.86 ± 0.04	0.76 ± 0.05	0.75 ± 0.05	0.81 ± 0.04

Table 6: Detailed evaluation results of DP training with $\varepsilon = 2.04$, $\delta = 6 \cdot 10^{-6}$. The results show the average and individual AUROC, accuracy, specificity, and sensitivity values for each label tested on $n = 39,809$ test images. The training dataset includes $n = 153,502$ images.

	AUROC	Accuracy	Specificity	Sensitivity
Cardiomegaly	0.80 ± 0.00	0.72 ± 0.00	0.69 ± 0.02	0.76 ± 0.02
Congestion	0.80 ± 0.00	0.70 ± 0.02	0.69 ± 0.02	0.75 ± 0.02
Pleural Effusion Right	0.90 ± 0.00	0.80 ± 0.01	0.79 ± 0.02	0.86 ± 0.02
Pleural Effusion Left	0.86 ± 0.00	0.73 ± 0.02	0.72 ± 0.02	0.83 ± 0.02
Pneumonic Infiltration Right	0.89 ± 0.00	0.80 ± 0.02	0.80 ± 0.03	0.81 ± 0.03
Pneumonic Infiltration Left	0.89 ± 0.00	0.79 ± 0.01	0.79 ± 0.02	0.83 ± 0.02
Atelectasis Right	0.84 ± 0.00	0.74 ± 0.02	0.74 ± 0.02	0.80 ± 0.02
Atelectasis Left	0.82 ± 0.00	0.70 ± 0.01	0.69 ± 0.02	0.79 ± 0.02
Average	0.85 ± 0.04	0.75 ± 0.04	0.74 ± 0.05	0.80 ± 0.04

Table 7: Detailed evaluation results of DP training with $\varepsilon = 1.06$, $\delta = 6 \cdot 10^{-6}$. The results show the average and individual AUROC, accuracy, specificity, and sensitivity values for each label tested on $n = 39,809$ test images. The training dataset includes $n = 153,502$ images.

	AUROC	Accuracy	Specificity	Sensitivity
Cardiomegaly	0.79 ± 0.00	0.72 ± 0.00	0.69 ± 0.01	0.74 ± 0.01
Congestion	0.79 ± 0.00	0.67 ± 0.02	0.66 ± 0.02	0.78 ± 0.02
Pleural Effusion Right	0.89 ± 0.00	0.77 ± 0.01	0.76 ± 0.02	0.86 ± 0.02
Pleural Effusion Left	0.84 ± 0.00	0.71 ± 0.02	0.70 ± 0.03	0.84 ± 0.03
Pneumonic Infiltration Right	0.88 ± 0.00	0.80 ± 0.01	0.80 ± 0.02	0.79 ± 0.02
Pneumonic Infiltration Left	0.88 ± 0.00	0.77 ± 0.02	0.77 ± 0.03	0.83 ± 0.03
Atelectasis Right	0.83 ± 0.00	0.74 ± 0.01	0.73 ± 0.01	0.79 ± 0.01
Atelectasis Left	0.81 ± 0.00	0.70 ± 0.03	0.70 ± 0.03	0.77 ± 0.03
Average	0.84 ± 0.04	0.73 ± 0.04	0.73 ± 0.05	0.80 ± 0.04

Table 8: Detailed evaluation results of DP training with $\varepsilon = 0.54$, $\delta = 6 \cdot 10^{-6}$. The results show the average and individual AUROC, accuracy, specificity, and sensitivity values for each label tested on $n = 39,809$ test images. The training dataset includes $n = 153,502$ images.

	AUROC	Accuracy	Specificity	Sensitivity
Cardiomegaly	0.79 ± 0.00	0.71 ± 0.00	0.67 ± 0.01	0.75 ± 0.01
Congestion	0.78 ± 0.00	0.68 ± 0.02	0.68 ± 0.02	0.74 ± 0.02
Pleural Effusion Right	0.88 ± 0.00	0.77 ± 0.01	0.77 ± 0.02	0.83 ± 0.02
Pleural Effusion Left	0.84 ± 0.00	0.73 ± 0.01	0.72 ± 0.02	0.80 ± 0.02
Pneumonic Infiltration Right	0.87 ± 0.00	0.79 ± 0.01	0.79 ± 0.02	0.79 ± 0.02
Pneumonic Infiltration Left	0.88 ± 0.00	0.79 ± 0.01	0.79 ± 0.01	0.81 ± 0.01
Atelectasis Right	0.82 ± 0.00	0.73 ± 0.02	0.73 ± 0.02	0.77 ± 0.02
Atelectasis Left	0.80 ± 0.00	0.71 ± 0.02	0.71 ± 0.02	0.75 ± 0.02
Average	0.83 ± 0.04	0.74 ± 0.04	0.73 ± 0.05	0.78 ± 0.04

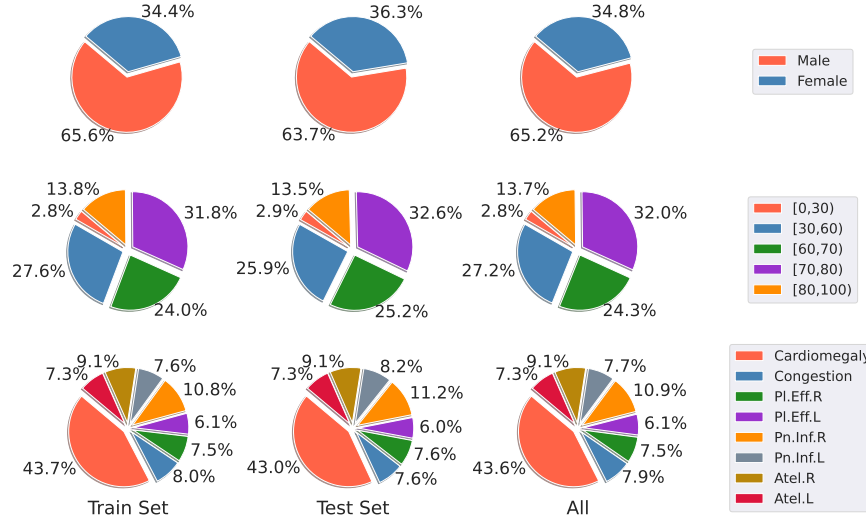
Table 9: Detailed evaluation results of DP training with $\varepsilon = 0.29$, $\delta = 6 \cdot 10^{-6}$. The results show the average and individual AUROC, accuracy, specificity, and sensitivity values for each label tested on $n = 39,809$ test images. The training dataset includes $n = 153,502$ images.

PDAC														
	Total		Male		Female		Youngest 25%		Second 25%		Third 25%		Oldest 25%	
ε	μ	σ	μ	σ	μ	σ	μ	σ	μ	σ	μ	σ	μ	σ
0.29	24.86	10.7	23.86	9.6	25.54	14.0	20.29	23.9	15.97	7.9	32.10	8.8	27.78	12.0
0.54	11.37	3.2	11.23	3.4	10.82	4.2	8.70	8.7	4.86	2.4	19.14	7.0	10.42	2.1
1.06	5.97	1.7	5.96	1.6	6.06	2.0	2.90	2.5	1.39	2.4	11.11	3.7	6.25	2.1
2.04	2.70	0.9	2.46	0.6	3.03	1.5	1.45	2.5	1.39	1.2	3.09	1.1	4.17	3.6
4.71	1.73	1.0	1.40	0.6	2.16	1.5	1.45	2.5	0.69	1.2	1.85	0.0	2.78	1.2
5.0	2.31	2.0	1.75	1.2	3.03	3.0	1.45	2.5	1.39	2.4	2.47	1.1	3.47	2.4
6.0	3.08	2.3	2.46	2.2	3.90	2.6	1.45	2.5	2.08	2.1	3.70	3.2	4.17	2.1
7.0	1.54	1.2	1.40	1.6	1.73	1.5	0.00	0.0	0.69	1.2	2.47	2.8	2.08	2.1
8.0	0.58	0.6	0.00	0.0	1.30	1.3	0.00	0.0	1.39	2.4	0.00	0.0	0.69	1.2
Non-private	0.77	0.7	0.00	0.0	1.73	1.5	0.00	0.0	2.08	2.1	0.62	1.1	0.00	0.0

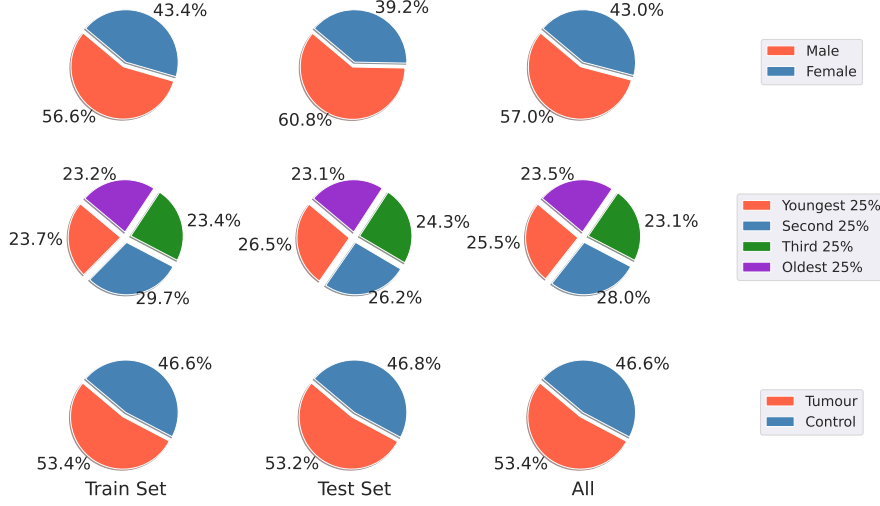
Table 10: Underdiagnosis rates of subgroups. Underdiagnosis rate is the false positive rate of non-tumour cases. μ denotes the mean underdiagnosis rate for a certain subgroup, while σ denotes the standard deviation.

	Tumor		Control		PtD	
N Test	173		152			
ε	μ	σ	μ	σ	μ	σ
0.29	75.14	10.7	85.09	2.3	-9.94	13.0
0.54	88.63	3.2	86.40	2.5	2.23	5.4
1.06	94.03	1.7	85.53	3.5	8.50	4.7
2.04	97.30	0.9	87.94	1.0	9.36	0.4
4.71	98.27	1.0	90.57	1.9	7.70	2.9
5.0	97.69	2.0	91.01	2.1	6.68	4.1
6.0	96.92	2.3	91.89	1.7	5.03	4.0
7.0	98.46	1.2	90.79	1.7	7.67	2.8
8.0	99.42	0.6	95.39	3.7	4.03	3.5
∞	99.23	0.7	97.81	1.5	1.42	1.3

Table 11: Per Diagnosis Accuracy on the PDAC dataset. PtD is the statistical parity difference between the tumor and control group. μ denotes the mean, σ the standard deviation over three runs.



(a) UKA-CXR dataset



(b) PDAC dataset

Figure 7: Visual overview of the distribution over subgroups

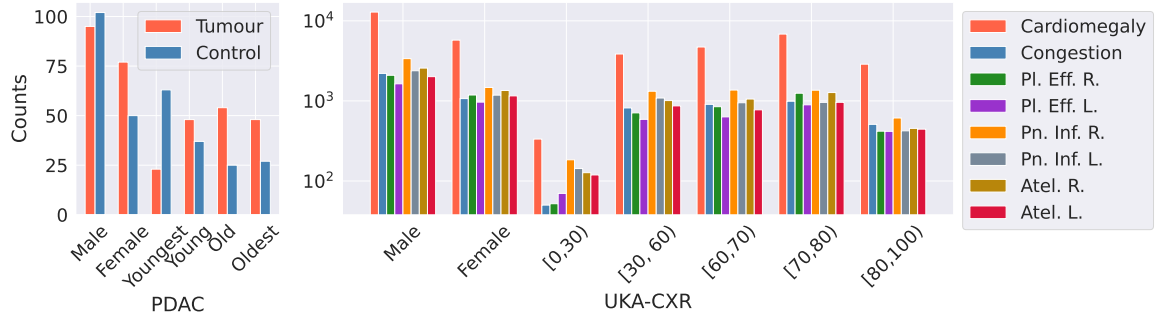


Figure 8: Distribution of labels within subgroups

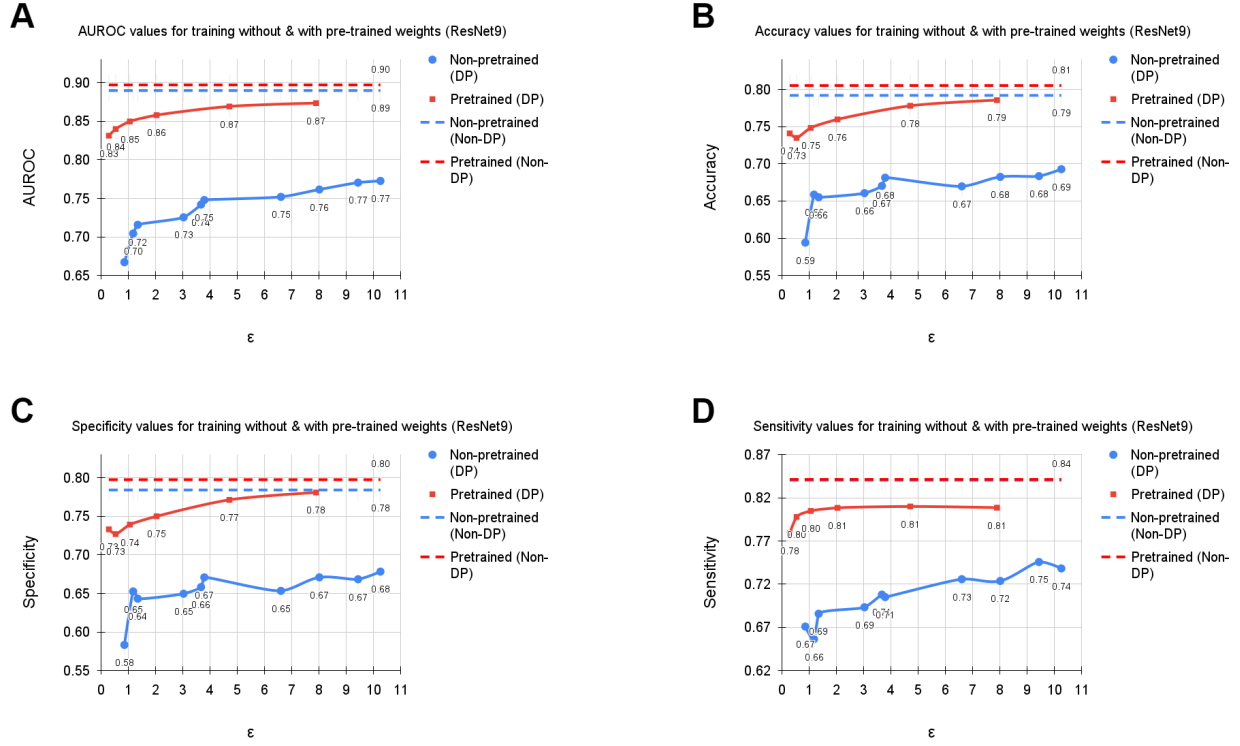


Figure 9: Average results of DP training with different ϵ values for $\delta = 6 \cdot 10^{-6}$ using pre-trained weights versus training from scratch. The curves show the average (A) AUROC, (B) accuracy, (C) specificity, and (D) sensitivity values over all labels, including cardiomegaly, congestion, pleural effusion right, pleural effusion left, pneumonic infiltration right, pneumonic infiltration left, atelectasis right, and atelectasis left tested on $N = 39\,809$ test images. The training dataset includes $N = 153\,502$ images. Note, that the AUROC is monotonically increasing, while sensitivity, specificity, and accuracy exhibit more variation. This is due to the fact that all training processes were optimized for the AUROC. Dashed lines correspond to the non-private training results depicted as upper bounds. The pre-training was done using the MIMIC-CXR dataset with $N = 210\,652$ images.

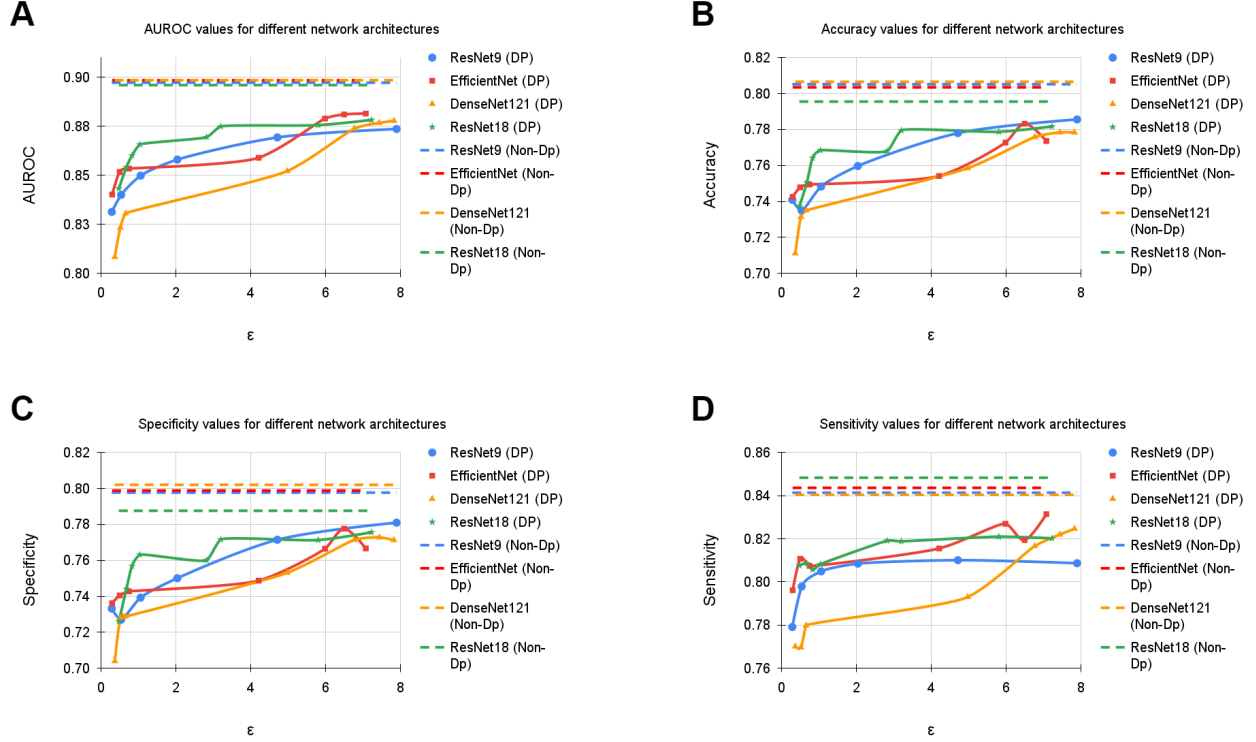


Figure 10: Average results of training with DP with different ε values for $\delta = 6 \cdot 10^{-6}$ using different network architectures. The curves show the average (A) AUROC, (B) accuracy, (C) specificity, and (D) sensitivity values over all labels, including cardiomegaly, congestion, pleural effusion right, pleural effusion left, pneumonic infiltration right, pneumonic infiltration left, atelectasis right, and atelectasis left tested on $N = 39\,809$ test images. The training dataset includes $N = 153\,502$ images. Note, that the AUROC is monotonically increasing, while sensitivity, specificity, and accuracy exhibit more variation. This is due to the fact that all training processes were optimized for the AUROC. Dashed lines correspond to the non-private training results depicted as upper bounds.

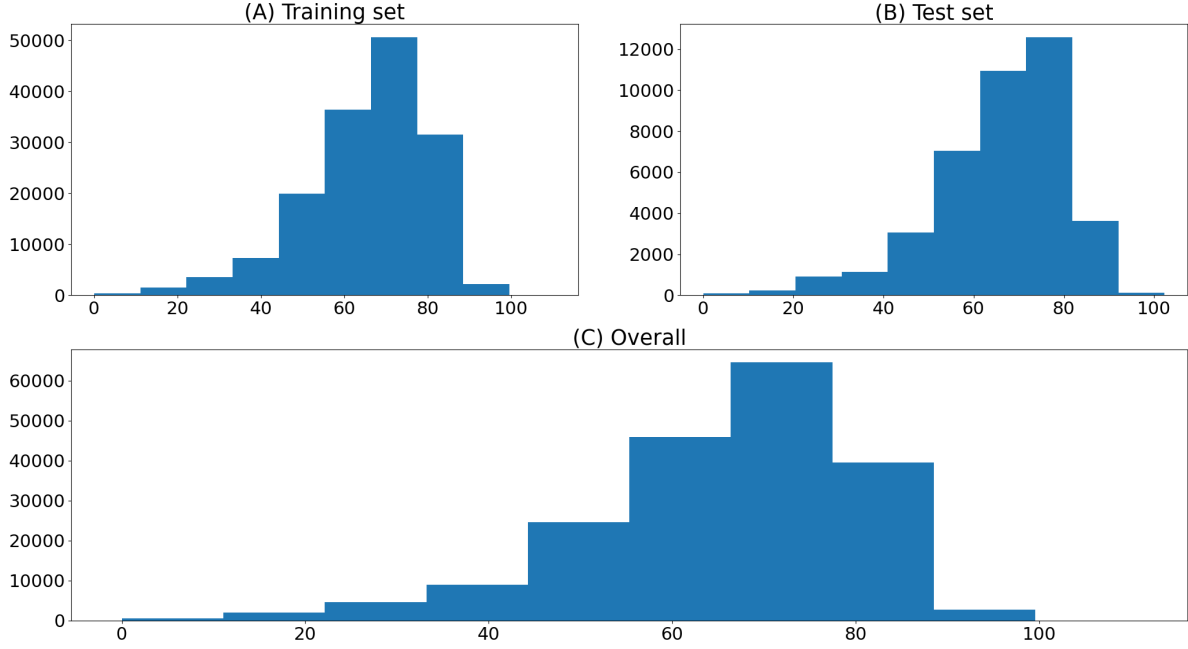


Figure 11: Age histogram of the UKA-CXR dataset. (A) Training set. (B) Test set. (C) Overall.

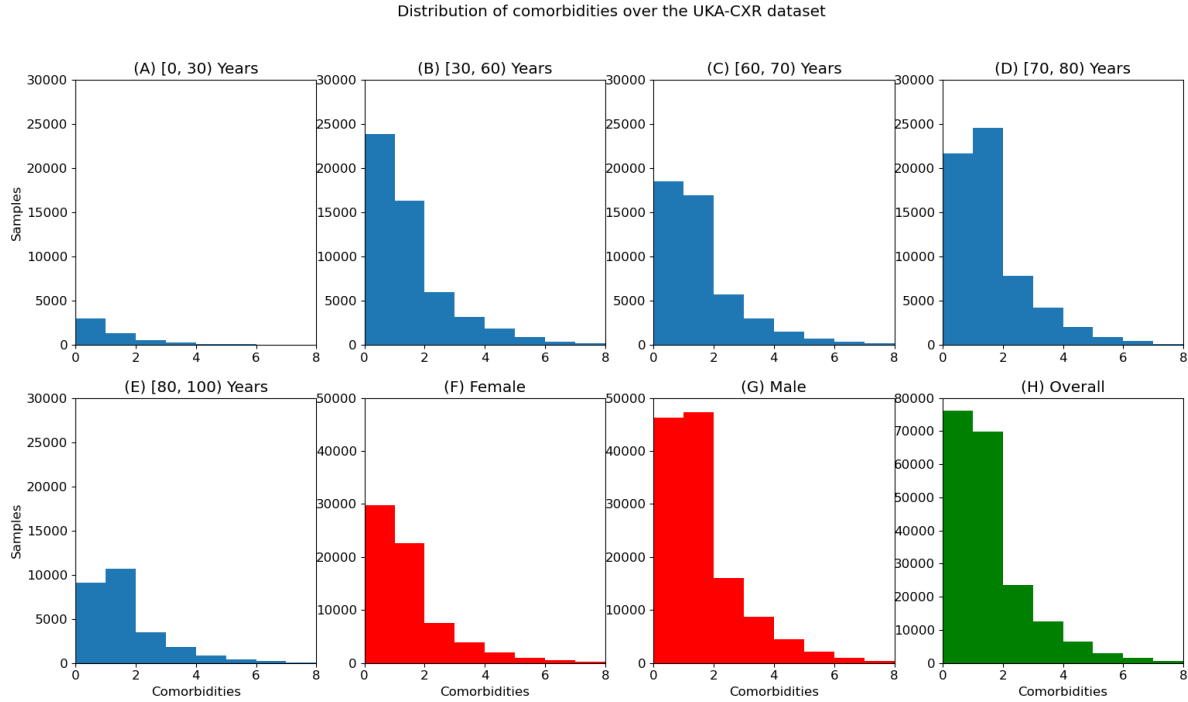


Figure 12: Distribution of comorbidities over the UKA-CXR dataset. Histograms of comorbidities are given for different subsets of the dataset including subjects aging in the range of (A) [0, 30) years old with a mean of 0.8 ± 1.2 comorbidities, (B) [30, 60) years old with a mean of 1.0 ± 1.3 comorbidities, (C) [60, 70) years old with a mean of 1.1 ± 1.3 comorbidities, (D) [70, 80) years old with a mean of 1.1 ± 1.2 comorbidities, (E) [80, 100) years old with a mean of 1.1 ± 1.3 comorbidities, as well as (F) females with a mean of 1.0 ± 1.2 comorbidities, (G) males with a mean of 1.1 ± 1.3 comorbidities, and (H) overall with a mean of 1.1 ± 1.3 comorbidities.

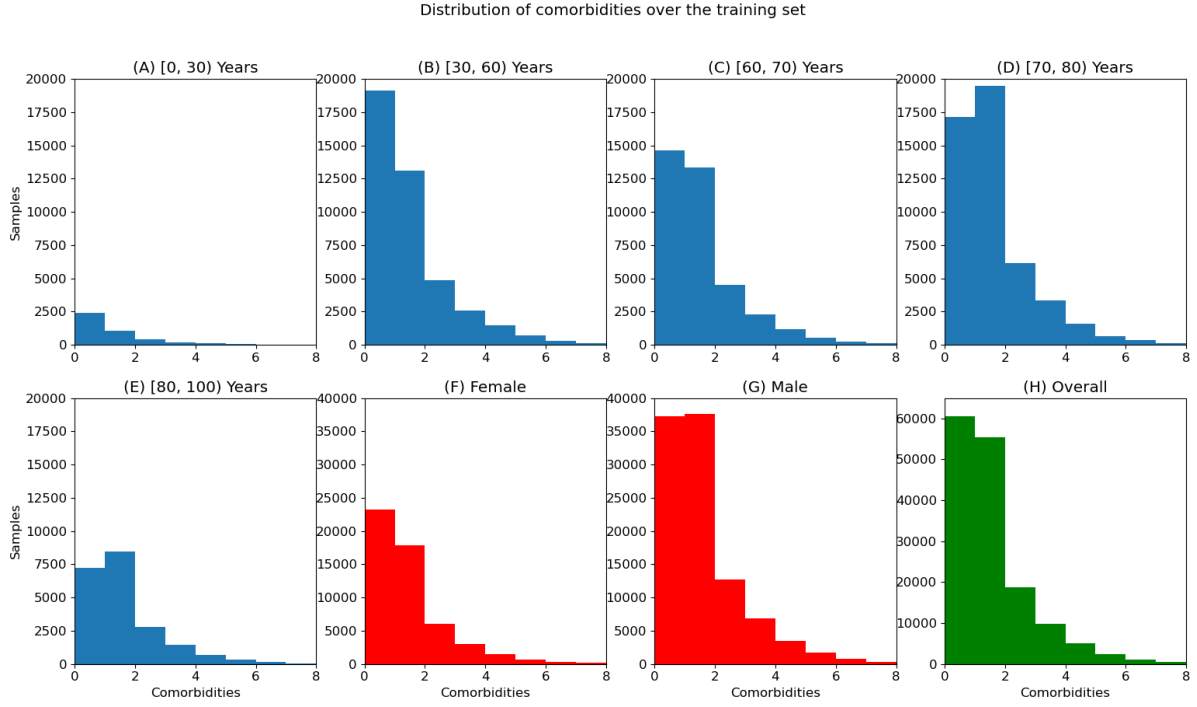


Figure 13: Distribution of comorbidities over the training set. Histograms of comorbidities are given for different subsets of the training set including subjects aging in the range of (A) [0, 30) years old with a mean of 0.8 ± 1.2 comorbidities, (B) [30, 60) years old with a mean of 1.0 ± 1.3 comorbidities, (C) [60, 70) years old with a mean of 1.1 ± 1.3 comorbidities, (D) [70, 80) years old with a mean of 1.1 ± 1.2 comorbidities, (E) [80, 100) years old with a mean of 1.1 ± 1.3 comorbidities, as well as (F) females with a mean of 1.0 ± 1.2 comorbidities, (G) males with a mean of 1.1 ± 1.3 comorbidities, and (H) overall training set with a mean of 1.1 ± 1.3 comorbidities.

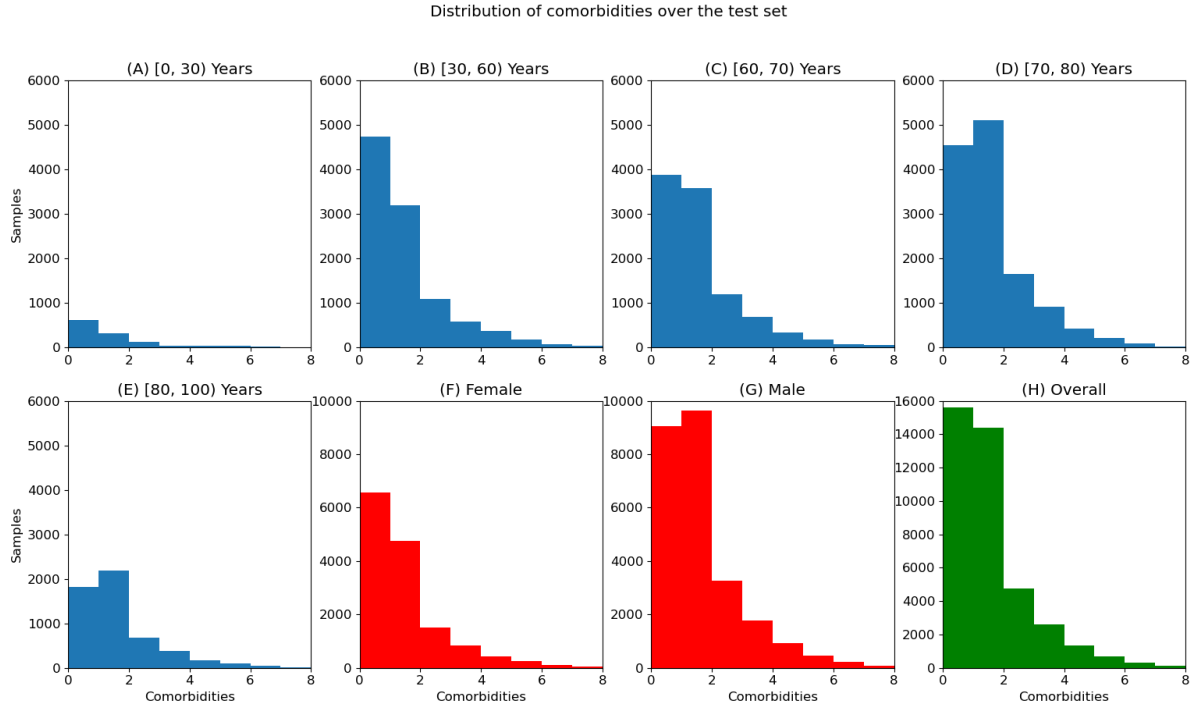


Figure 14: Distribution of comorbidities over the test set. Histograms of comorbidities are given for different subsets of the test set including subjects aging in the range of (A) $[0, 30)$ years old with a mean of 0.9 ± 1.4 comorbidities, (B) $[30, 60)$ years old with a mean of 1.0 ± 1.3 comorbidities, (C) $[60, 70)$ years old with a mean of 1.1 ± 1.3 comorbidities, (D) $[70, 80)$ years old with a mean of 1.1 ± 1.2 comorbidities, (E) $[80, 100)$ years old with a mean of 1.1 ± 1.3 comorbidities, as well as (F) females with a mean of 1.0 ± 1.3 comorbidities, (G) males with a mean of 1.1 ± 1.3 comorbidities, and (H) overall test set with a mean of 1.1 ± 1.3 comorbidities.

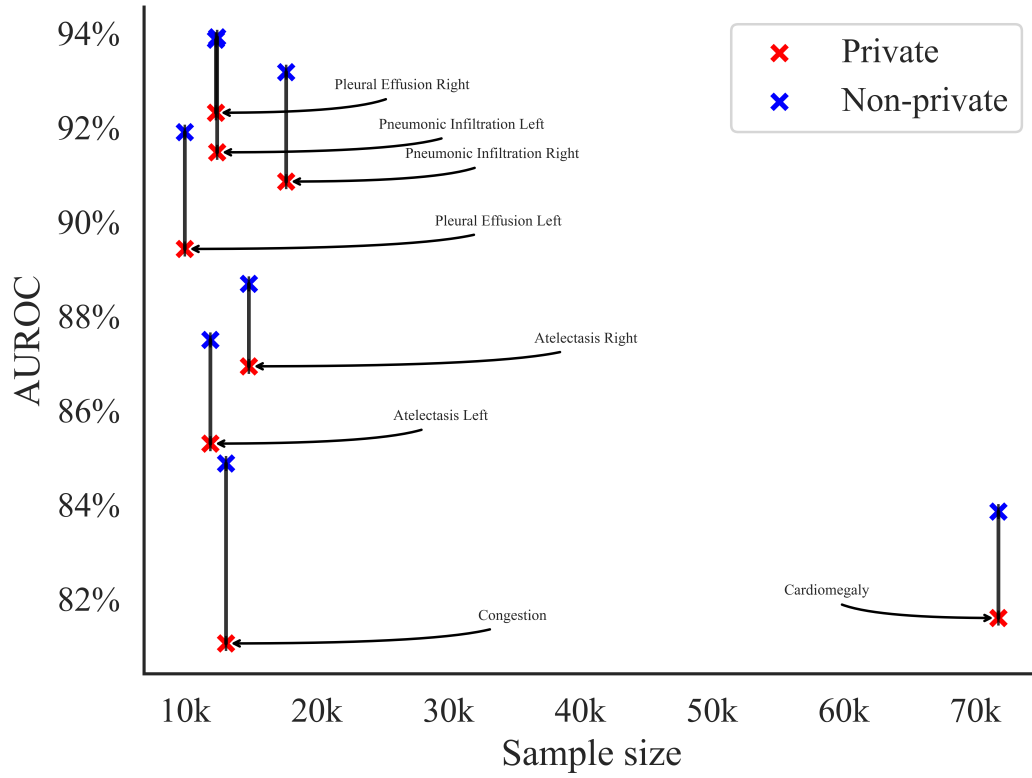


Figure 15: Relation of sample size to training performance for private and performance loss compared to non private training. Each dot marks the performance on the test set on one diagnosis of the private model at $\varepsilon = 7.89$ (compare Figure 2). Colors indicate the performance loss compared to the non private model.

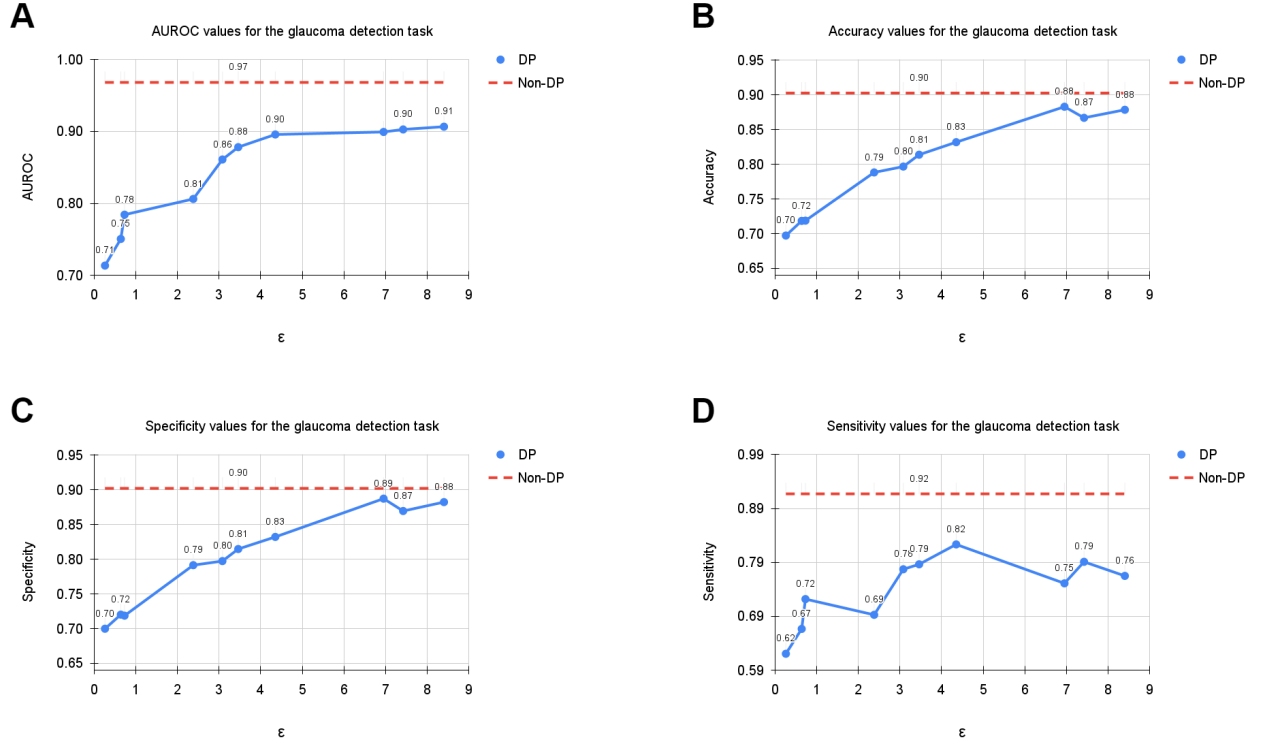


Figure 16: Evaluation results of the Glaucoma detection task [55] for training with DP with different ϵ values for $\delta = 6 \cdot 10^{-6}$. The curves show the (A) AUROC, (B) accuracy, (C) specificity, and (D) sensitivity values tested on $N = 20\,268$ test images. The training dataset includes $N = 81\,086$ images. Note, that the AUROC is monotonically increasing, while sensitivity, specificity, and accuracy exhibit more variation. This is due to the fact that all training processes were optimized for the AUROC. Dashed lines correspond to the non-private training results depicted as upper bounds.